International Journal for Numerical Methods in Engineering

WILEY

RESEARCH ARTICLE OPEN ACCESS

Robust and Efficient FFT-Based Solvers for Unit-Cell Problems With Voids and Pores Under Displacement Boundary Conditions

Lennart Risthaus[1] | Matti Schneider[1,2]

[1]University of Duisburg-Essen, Institute of Engineering Mathematics, Duisburg, Germany | [2]Fraunhofer Institute for Industrial Mathematics ITWM, Kaiserslautern, Germany

Correspondence: Matti Schneider (matti.schneider@uni-due.de)

Received: 4 March 2025 | **Revised:** 11 August 2025 | **Accepted:** 28 August 2025

Funding: This work was supported by European Research Council within the Horizon Europe program—Grant No. 101040238.

Keywords: Dirichlet boundary conditions | discrete cosine transform | discrete sine transform | FFT-based computational micromechanics | staggered grid

ABSTRACT

There is a variety of microstructured materials that involve voids and pores, for example, high-porosity foams, mechanical metamaterials, or composites involving defects due to damage and cracking, respectively. Computational methods based on the fast Fourier transform (FFT) typically face convergence problems for such microstructures unless specific discretizations are used, most prominently the discretization on the staggered grid. FFT-based methods were originally developed for periodic boundary conditions, and recent work provided extensions to Dirichlet and Neumann boundary conditions on the unit cube faces by utilizing dedicated sine and cosine series. Unfortunately, such approaches were only developed for discretizations that fail to converge for complex porous microstructures. The article at hand closes this gap by constructing the appropriate Eshelby-Green operator for the displacement gradient associated with the staggered grid discretization and Dirichlet boundary conditions. The eponymous staggering of the displacement variables infers certain challenges to be resolved, that is, the construction is significantly more difficult than for the cases discussed in the literature. However, our innovative techniques permit treating the class of microporous materials—which have a wide range of applicability—in a robust and efficient way. We showcase the superiority of the novel techniques via dedicated computational experiments.

1 | Introduction

1.1 | State of the Art

Computational homogenization methods enable designing components made of materials with a heterogeneous microstructure without having to resolve the microstructure details. Fast Fourier Transform (FFT)-based solvers based

on the Lippmann-Schwinger equation permit the computation of the homogenized mechanical properties. The efficiency of this approach, established by Moulinec and Suquet [1, 2], is based on the following: No system matrix needs to be assembled/stored, and the iteration counts of the associated solvers are bounded independently of the resolution. The original solver, called Basic Scheme, introduced by Moulinec-Suquet [1, 2] may be interpreted as a gradient descent scheme [3]. Based on this insight, other gradient-type methods were developed, such as the Barzilai-Borwein method [4, 5], Nesterov's method [6, 7] as well as linear [8–10] and nonlinear conjugate gradient (CG) methods [11]. Other solution schemes include Newton methods [3, 12] and Quasi-Newton methods [13, 14]. Polarization methods [15–17] represent another class of powerful solution approaches for highly nonlinear problems, like small-strain crystal viscoplasticity [18]. FFT-based homogenization methods were originally introduced in a small strain setting, but given the efficiency of the approach, they were extended to various problem settings, such as fracture [19–21], fluid problems [22–24] or wave propagation [25, 26]. The strategy for treating finite strain problems [3, 12] is at the center of the current publication's key ideas.

The discretization by Moulinec and Suquet may be interpreted as a non-conforming Fourier-Galerkin method, that is, it uses trigonometric polynomials as ansatz functions but relies upon the trapezoid rule for (inexact) quadrature [27]. Sharp convergence estimates for the Moulinec-Suquet discretization upon grid refinement are available [28]. These show that, for materials with finite contrast, the Moulinec-Suquet discretization converges with the same rate as Finite Element (FE) discretizations on a regular grid. However, the Moulinec-Suquet discretization suffers from two fundamental limitations:

- The discretization shows ringing artifacts [29], which are caused by Gibbs' phenomenon inherent to approximating discontinuous fields by trigonometric polynomials. This drawback may be remedied by using discretization schemes such as finite difference discretizations [30, 31] with special cases like the staggered grid [32] or the rotated staggered grid [33]. In the context of FFT-based homogenization approaches, on a regular grid, FE [34–36] discretizations may eliminate artifacts by employing fully integrated Q_1 [37–39] or reduced integration Q_1 elements with hourglass control [40, 41]. Finite volume [42, 43] discretizations serve as the third category of discretizations introduced to reduce artifacts in the local solution fields. Only for certain laminate microstructure types, a Radon transform-based discretization [44, 45] may eliminate all ringing artifacts.
- The discretized cell problem becomes ill-conditioned if voids or pores with zero stiffness are present in the microstructure. Examples for such microstructures include high-porosity foams [46, 47], porous ceramics [48, 49], and sand grain microstructures [50]. Finite difference or fully integrated FE discretizations mitigate this problem [51]. However, fully integrated finite elements need to employ more than one integration point per element, which is detrimental to performance, especially when evaluating nonlinear material laws [52].

Noticeably, the staggered grid discretization [32] remedies both limitations. A more complete overview of FFT-based homogenization methods is found in recent review articles [52–54].

By nature of the discrete Fourier transform, FFT-based homogenization methods inherently impose periodic boundary conditions on the displacement fluctuation. For random microstructures, the apparent properties of a volume element (VE) computed with periodic boundary conditions yield a compromise between the overestimated properties of Dirichlet (or displacement) boundary conditions and the underestimated properties of Neumann (or stress) boundary conditions [55]. Nevertheless, certain problem settings require non-periodic boundary conditions, such as the simulation of compression or microindentation experiments [56, 57].

To enforce Dirichlet boundary conditions, penalty methods [56–58] may be used. These come with the drawback of an artificially increased material contrast, that is, the ratio of the highest and the lowest stiffness within the microstructure. Alternatively, primal-dual formulations involving Lagrange multipliers [26, 59] allow imposing Dirichlet boundary conditions. However, the number of degrees of freedom of the system is increased and the emerging indefinite systems are hard to precondition efficiently [60].

Recently, a third strategy for enforcing non-periodic boundary conditions for FFT-based homogenization was explored: Using sine or cosine transforms instead of the Fourier transform permits representing fields with non-periodic boundary conditions [61]. A more or less straightforward replacement of the Fourier transform by the discrete equivalents of the sine and cosine transforms was successfully implemented for thermal conductivity [62–64], where any desired combination of boundary conditions may be obtained by symmetry considerations [65, 66]. Recently, an extension of this approach to Finel's discretization [67] was proposed [68]. On the other hand, for small-strain mechanics, a naive replacement is only

possible for certain load cases, such as mixed uniform boundary conditions [69–71]. At small strains and for Dirichlet boundary conditions, the traditional strategy to construct Green's operator does not work. More precisely, due to a mixed occurrence of non-orthogonal sine and cosine terms, upon sine or cosine transform, there is no block structure of the reference problem—like for periodic or mixed uniform boundary conditions—that is easily inverted. Prior work by the authors [72–74] introduced the idea of imposing Dirichlet boundary conditions by using a finite-strain preconditioner in a small-strain context for FFT-based solvers. Alternatively, this approach may be interpreted as using a (vector-valued version of) thermal-conductivity version of the Lippmann-Schwinger equation for small-strain mechanics, as well. This strategy generalizes to other non-periodic boundary conditions [58, 65, 75].

1.2 | Contributions

In the case of periodic boundary conditions, the (non-rotated) staggered grid discretization [76, 77], introduced for FFT-based solvers by Schneider et al. [32], ensures convergent solvers for microstructures that include void phases. For the latter, many other discretization schemes, such as the Moulinec-Suquet discretization or the *rotated* staggered grid (Q1R), do not lead to convergence, in general. Additionally, the staggered grid discretization is free of ringing and checkerboard artifacts, which significantly degrade the quality of the local solution fields generated by other discretization schemes. In this contribution, we introduce a scheme to impose Dirichlet boundary conditions for the staggered grid discretization [32] based on the bottom-up approach [72, 73]. For this approach, based on the desired boundary conditions, the Discrete Fourier Transform (DFT) employed in a periodic setting is replaced by a Discrete Cosine Transform (DCT) or Discrete Sine Transform (DST) in conjunction with an update of the algorithmic framework.

A critical reason for the stability and robustness of the staggered grid is the eponymous staggered placement of the displacement degrees of freedom for mechanical problems. However, this co-located arrangement increases the technical difficulty of setting up associated solvers with non-periodic boundary conditions. We elaborate on the difficulties and our ideas in Section 2, where we focus on vanishing Dirichlet data for the displacement-fluctuation field. More precisely, in contrast to mixed uniform boundary conditions, the *tangential* displacements need to be forced to zero half a voxel *inside* the domain. The locations of the different components of the displacement fields, as well as their gradients, are illustrated in Figure 1. Using the bottom-up approach as well as a careful selection of the proper boundary values, we introduce a scheme to evaluate the Eshelby-Green operator. The specific steps to construct the Eshelby-Green operator are derived and listed in Section 3.

Finally, in Section 4, we investigate the performance of the staggered grid discretization with Dirichlet boundary conditions on the example of four types of microstructures with increasing computational difficulty, starting with a single spherical inclusion and a bicontinuous stochastic microstructure, both with finite material contrast. We study a 3D-printed sand

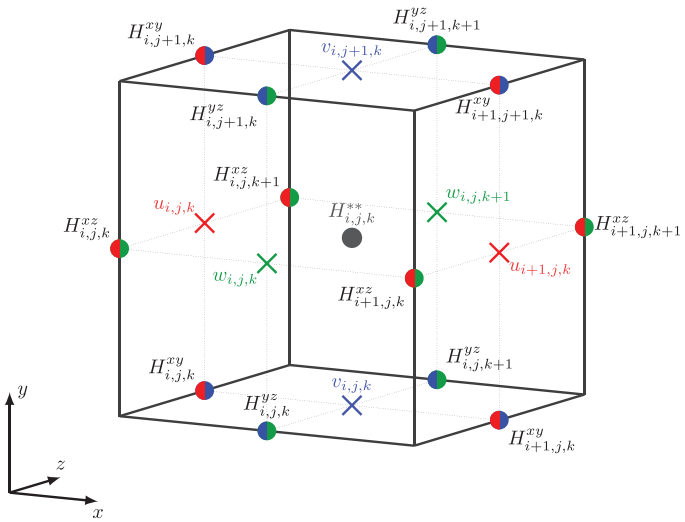

FIGURE 1 | A single voxel of the staggered grid discretization with locations of the associated degrees of freedom marked by crosses. The normal components are shown as black circles with H^{**} representing the normal gradient components H^{xx}, H^{yy}, and H^{zz}. Locations of the shear components are marked as bi-color circles with colors corresponding to the contributing displacements.

core microstructure with infinite material contrast, where complex sand grains are bound together by inorganic sand in an anisotropic additive-manufacturing process [50]. To conclude, we examine a dry foam microstructure, which is a microstructure with infinite contrast and low volume fraction of solid material, usually posing a challenge for FFT-based solvers with discretizations not based on the staggered grid.

2 | Dirichlet Boundary Conditions and the Staggered Grid

2.1 | The Continuous Problem

On a rectangular unit cell

$$Y = \left[0, L_1\right] \times \left[0, L_2\right] \times \left[0, L_3\right] \tag{1}$$

we suppose that a heterogeneous field $\mathbb{C} : Y \to (\mathbb{R}^3)^{\otimes 4}$ of elasticity tensors is given. We assume that this field satisfies both minor and major symmetries, that is, the conditions

$$\mathbb{C}_{ijk\ell} = \mathbb{C}_{jik\ell} = \mathbb{C}_{ij\ell k} = \mathbb{C}_{k\ell ij}, \quad i, j, k, \ell \in \{1, 2, 3\} \tag{2}$$

are satisfied. For a given mean strain

$$\overline{\boldsymbol{\varepsilon}} \in \mathrm{Sym}(3) \equiv \left\{ \tilde{\boldsymbol{H}} \in \mathbb{R}^{3\times 3} \middle| \tilde{\boldsymbol{H}}^T = \tilde{\boldsymbol{H}} \right\} \tag{3}$$

we seek a displacement fluctuation field

$$\boldsymbol{u} \in H_0^1(Y)^3 \tag{4}$$

which vanishes on the boundary ∂Y and satisfies the equilibrium equation

$$\mathrm{div}\left[\mathbb{C} : (\overline{\boldsymbol{\varepsilon}} + \nabla \boldsymbol{u})\right] = \boldsymbol{0} \tag{5}$$

without volume forces or inertial terms.

For the work at hand and with FFT-based computational resolution in mind, we rewrite Equation (5) as an equivalent Lippmann-Schwinger equation. For Dirichlet boundary conditions (4), a formulation on the full displacement gradient instead of the symmetrized gradient is advised. Therefore, we consider a reference "material" $\mathbb{C}^0 \in (\mathbb{R}^3)^{\otimes 4}$ with major but without minor symmetries. More precisely, we fix the simple reference "material"

$$\mathbb{R}^{3\times 3} \ni \tilde{\boldsymbol{H}} \mapsto \alpha_0 \tilde{\boldsymbol{H}} \in \mathbb{R}^{3\times 3} \tag{6}$$

with a positive modulus α_0. We consider the associated Green's operator

$$\boldsymbol{G}_0 : H_0^{-1}(Y)^3 \to H_0^1(Y)^3, \quad \boldsymbol{f} \mapsto \boldsymbol{G}_0 \boldsymbol{f} \tag{7}$$

which is implicitly defined so that the equivalence

$$\boldsymbol{u} = \boldsymbol{G}^0 \boldsymbol{f} \Leftrightarrow \mathrm{div}\, \mathbb{C}^0 : \nabla \boldsymbol{u} = \boldsymbol{f} \tag{8}$$

holds for any suitable force field $\boldsymbol{f} \in H_0^{-1}(Y)^3$ with vanishing mean. With this notation at hand, by introducing the Eshelby-Green operator

$$\boldsymbol{\Gamma}_0 \equiv \nabla \boldsymbol{G}_0\, \mathrm{div} \tag{9}$$

the equivalent Lippmann-Schwinger equation

$$\boldsymbol{H} = \overline{\boldsymbol{\varepsilon}} - \boldsymbol{\Gamma}_0 : \left[\left(\mathbb{C} - \mathbb{C}_0\right) : \boldsymbol{H}\right] \tag{10}$$

for the field

$$\boldsymbol{H} \in L^2(Y; \mathbb{R}^{3\times 3}) \tag{11}$$

is obtained as usual [72]. The associated fixed-point scheme

$$\boldsymbol{H}^{k+1} = \overline{\boldsymbol{\varepsilon}} - \boldsymbol{\Gamma}_0 : \left[\left(\mathbb{C} - \mathbb{C}_0\right) : \boldsymbol{H}^k\right], \quad k \in \mathbb{N}_+ \tag{12}$$

is called the Basic Scheme [1, 2].

2.2 | The Staggered Grid Discretization

We discretize the rectangular cell Y (1) with $N_i \in \mathbb{N}_+$ $(i = 1, 2, 3)$ voxels in each coordinate direction.

For the staggered grid discretization, we suppose that the displacement degrees of freedom are given on the *faces* of the voxel, see Figure 1. Thus, the displacement fluctuation field (4) is represented on the discrete level by three scalar fields

$$u : \{0, 1, \dots, N_1\} \times \{0, 1, \dots, N_2 - 1\} \times \{0, 1, \dots, N_3 - 1\} \to \mathbb{R} \tag{13}$$

$$v : \{0, 1, \dots, N_1 - 1\} \times \{0, 1, \dots, N_2\} \times \{0, 1, \dots, N_3 - 1\} \to \mathbb{R} \tag{14}$$

$$w : \{0, 1, \dots, N_1 - 1\} \times \{0, 1, \dots, N_2 - 1\} \times \{0, 1, \dots, N_3\} \to \mathbb{R} \tag{15}$$

which correspond to the displacements in x-, y- and z-direction, respectively. To these displacement values, we associate the following diagonal components of the displacement gradient $\boldsymbol{H}$

$$H^{xx}[\mathbf{j}] = \frac{u[\mathbf{j} + \boldsymbol{e}_1] - u[\mathbf{j}]}{h_1} \tag{16}$$

$$H^{yy}[\mathbf{j}] = \frac{v[\mathbf{j} + \boldsymbol{e}_2] - v[\mathbf{j}]}{h_2} \tag{17}$$

$$H^{zz}[\mathbf{j}] = \frac{w[\mathbf{j} + \boldsymbol{e}_3] - w[\mathbf{j}]}{h_3} \tag{18}$$

where $h_i = L_i/N_i$ $(i = 1, 2, 3)$ denotes the voxel length and the index $\mathbf{j}$ runs among the set of voxels

$$\mathbf{j} \in \{0, 1, \dots, N_1 - 1\} \times \{0, 1, \dots, N_2 - 1\} \times \{0, 1, \dots, N_3 - 1\} \tag{19}$$

The corresponding shear components of the displacement gradient read

$$H^{xy}[\mathbf{j}] = \frac{u[\mathbf{j}] - u[\mathbf{j} - \boldsymbol{e}_2]}{h_2} \tag{20}$$

$$H^{yx}[\mathbf{j}] = \frac{v[\mathbf{j}] - v[\mathbf{j} - \boldsymbol{e}_1]}{h_1} \tag{21}$$

$$H^{xz}[\mathbf{j}] = \frac{u[\mathbf{j}] - u[\mathbf{j} - \boldsymbol{e}_3]}{h_3} \tag{22}$$

$$H^{zx}[\mathbf{j}] = \frac{w[\mathbf{j}] - w[\mathbf{j} - \boldsymbol{e}_1]}{h_1} \tag{23}$$

$$H^{yz}[\mathbf{j}] = \frac{v[\mathbf{j}] - v[\mathbf{j} - \boldsymbol{e}_3]}{h_3} \tag{24}$$

$$H^{zy}[\mathbf{j}] = \frac{w[\mathbf{j}] - w[\mathbf{j} - \boldsymbol{e}_2]}{h_2} \tag{25}$$

where the index $\mathbf{j}$ runs through the set of voxels where the operations make sense, and we set $H^{ab}[\mathbf{j}] = 0$ otherwise. In fact, there is a certain ambiguity when indexing the shear components (20–25). We selected to put the indices to the bottom left, see Figure 1.

We enforce Dirichlet boundary conditions for the displacement fields (13–15), that is, we set

$$u[\mathbf{j}] = 0 \quad \text{if} \quad j_1 = 0 \quad \text{or} \quad j_1 = N_1 \quad \text{or} \quad j_2 = 0 \quad \text{or} \quad j_2 = N_2 - 1 \quad \text{or} \quad j_3 = 0 \quad \text{or} \quad j_3 = N_3 - 1 \tag{26}$$

for the u-displacement (13), and similarly for the v-displacement

$$v[\mathbf{j}] = 0 \quad \text{if} \quad j_1 = 0 \quad \text{or} \quad j_1 = N_1 - 1 \quad \text{or} \quad j_2 = 0 \quad \text{or} \quad j_2 = N_2 \quad \text{or} \quad j_3 = 0 \quad \text{or} \quad j_3 = N_3 - 1 \tag{27}$$

and the w-displacment

$$w[\mathbf{j}] = 0 \quad \text{if} \quad j_1 = 0 \quad \text{or} \quad j_1 = N_1 - 1 \quad \text{or} \quad j_2 = 0 \quad \text{or} \quad j_2 = N_2 - 1 \quad \text{or} \quad j_3 = 0 \quad \text{or} \quad j_3 = N_3 \tag{28}$$

Figure 2 shows a 2D sketch of a small staggered grid, where the nodes with Dirichlet boundary conditions are marked in a lighter color.

In contrast to the mixed uniform boundary conditions [70], which require the normal displacements at the interface to vanish, the Dirichlet boundary conditions enforce the tangential displacements to be zero, as well.

The linear elastic constitutive law is applied as follows. For a prescribed strain $\overline{\boldsymbol{\varepsilon}}$ and voxel-wise given small-strain stiffness tensors $\mathbb{C}[\mathbf{j}]$, we first build the voxel-wise strain tensor $\boldsymbol{\varepsilon}[\mathbf{j}]$ with normal

$$\varepsilon^{aa}[\mathbf{j}] = \overline{\varepsilon}^{aa} + H^{aa}[\mathbf{j}] \quad \text{for} \quad a \in \{x, y, z\} \tag{29}$$

and shear components

$$\varepsilon^{ab}[\mathbf{j}] = \overline{\varepsilon}^{ab} + \frac{1}{2}\left(H^{ab}[\mathbf{j}] + H^{ab}[\mathbf{j}]\right) \quad \text{for} \quad ab \in \{yz, xz, xy\} \tag{30}$$

Then we compute the voxel-wise Cauchy stress tensor

$$\boldsymbol{\sigma}[\mathbf{j}] = \mathbb{C}[\mathbf{j}] : \boldsymbol{\varepsilon}[\mathbf{j}] \tag{31}$$

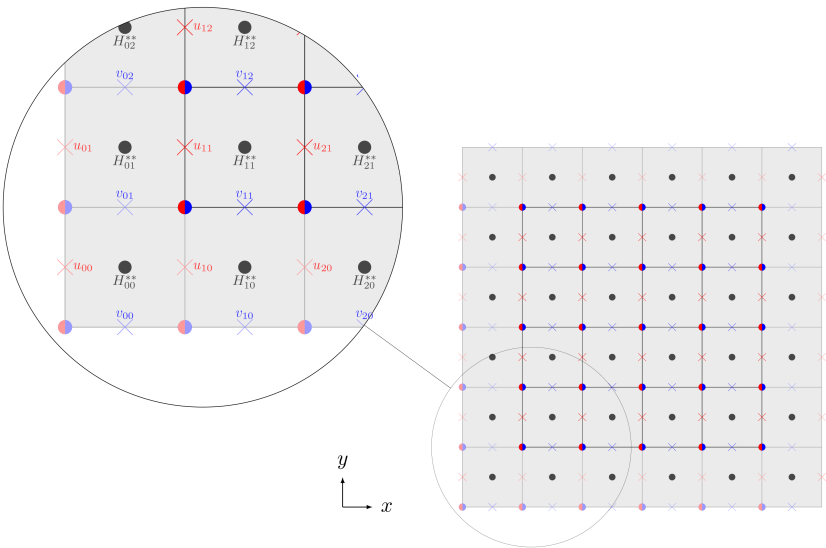

FIGURE 2 | Enforcing Dirichlet boundary conditions on a two-dimensional 6×6-grid—locations of the displacements are denoted by crosses. The normal components are shown as black circles with H^{**} representing both H^{xx} and H^{yy}. The in-plane locations of the shear components are denoted by bi-color circles. The fixed-displacement nodes are marked in a lighter color. Voxels unaffected by the boundary conditions are outlined in the center.

Finally, we switch back to the large-strain setting (10) and distribute the stress components suitably to the normal

$$P^{aa}[\mathbf{j}] = \sigma^{aa}[\mathbf{j}], \quad a \in \{x, y, z\} \tag{32}$$

and the shear components

$$P^{ab}[\mathbf{j}] = \sigma^{ab}[\mathbf{j}] \quad \text{and} \quad P^{ba}[\mathbf{j}] = \sigma^{ab}[\mathbf{j}] \quad \text{for} \quad (a, b) \in \{(x, y), (x, z), (y, z)\} \tag{33}$$

where $\boldsymbol{P}$ stands for the Piola-Kirchhoff stress tensor.

For a given (potentially non-symmetric) stress tensor $\boldsymbol{P}$, we wish to compute its *divergence*, represented by the force vector $\boldsymbol{f}$—which is co-located with the displacement fields (13–15). Following the internal logic of the staggered grid, the divergence is computed as

$$f^x[\mathbf{j}] = \frac{P^{xx}[\mathbf{j}] - P^{xx}[\mathbf{j} - \boldsymbol{e}_1]}{h_1} + \frac{P^{xy}[\mathbf{j} + \boldsymbol{e}_2] - P^{xy}[\mathbf{j}]}{h_2} + \frac{P^{xz}[\mathbf{j} + \boldsymbol{e}_3] - P^{xz}[\mathbf{j}]}{h_3} \tag{34}$$

$$f^y[\mathbf{j}] = \frac{P^{yx}[\mathbf{j} + \boldsymbol{e}_1] - P^{yx}[\mathbf{j}]}{h_1} + \frac{P^{yy}[\mathbf{j}] - P^{yy}[\mathbf{j} - \boldsymbol{e}_2]}{h_2} + \frac{P^{yz}[\mathbf{j} + \boldsymbol{e}_3] - P^{yz}[\mathbf{j}]}{h_3} \tag{35}$$

$$f^z[\mathbf{j}] = \frac{P^{zx}[\mathbf{j} + \boldsymbol{e}_1] - P^{zx}[\mathbf{j}]}{h_1} + \frac{P^{zy}[\mathbf{j} + \boldsymbol{e}_2] - P^{zy}[\mathbf{j}]}{h_2} + \frac{P^{zz}[\mathbf{j}] - P^{zz}[\mathbf{j} - \boldsymbol{e}_3]}{h_3} \tag{36}$$

In particular, the balance Equation (5) takes the form

$$\boldsymbol{f}[\mathbf{j}] = \mathbf{0} \tag{37}$$

for all voxels $\mathbf{j}$ on the interior of the grid and $\boldsymbol{f} = \operatorname{div} \boldsymbol{P}$. A sketch of the handling of the nodes on the boundary is given in Figure 2, where the fixed nodes are denoted by the light-colored crosses.

2.3 | Computing Derivatives via Discrete Sine and Cosine Transforms

To satisfy the Dirichlet boundary conditions (26–28) exactly, we make an ansatz for the displacement fields (13–15) in terms of truncated sine polynomials:

$$u[\mathbf{j}] = \sum_{k_1=1}^{N_1-1} \sum_{k_2=1}^{N_2-2} \sum_{k_3=1}^{N_3-2} \hat{u}[\mathbf{k}] \sin\left(\pi \frac{j_1 k_1}{N_1}\right) \sin\left(\pi \frac{j_2 k_2}{N_2 - 1}\right) \sin\left(\pi \frac{j_3 k_3}{N_3 - 1}\right) \tag{38}$$

$$v[\mathbf{j}] = \sum_{k_1=1}^{N_1-2} \sum_{k_2=1}^{N_2-1} \sum_{k_3=1}^{N_3-2} \hat{v}[\mathbf{k}] \sin\left(\pi \frac{j_1 k_1}{N_1 - 1}\right) \sin\left(\pi \frac{j_2 k_2}{N_2}\right) \sin\left(\pi \frac{j_3 k_3}{N_3 - 1}\right) \tag{39}$$

$$w[\mathbf{j}] = \sum_{k_1=1}^{N_1-2} \sum_{k_2=1}^{N_2-2} \sum_{k_3=1}^{N_3-1} \hat{w}[\mathbf{k}] \sin\left(\pi \frac{j_1 k_1}{N_1 - 1}\right) \sin\left(\pi \frac{j_2 k_2}{N_2 - 1}\right) \sin\left(\pi \frac{j_3 k_3}{N_3}\right) \tag{40}$$

with the decomposition $\mathbf{k} = (k_1, k_2, k_3)$ and where the index $\mathbf{j}$ runs over the domain of the respective displacement fields (13–15). The ansatz is motivated by the number of degrees of freedom available and ensures the validity of the Dirichlet boundary conditions (26–28) automatically.

To compute an expression for the displacement gradient (16) at the voxel center, we observe

$$\begin{aligned} h_1 H^{xx}[\mathbf{j}] &= u[\mathbf{j} + \boldsymbol{e}_1] - u[\mathbf{j}] \\ &= \sum_{k_1=1}^{N_1-1} \sum_{k_2=1}^{N_2-2} \sum_{k_3=1}^{N_3-2} \hat{u}[\mathbf{k}] \left[\sin\left(\pi \frac{(j_1+1)k_1}{N_1}\right) - \sin\left(\pi \frac{j_1 k_1}{N_1}\right)\right] \sin\left(\pi \frac{j_2 k_2}{N_2 - 1}\right) \sin\left(\pi \frac{j_3 k_3}{N_3 - 1}\right) \end{aligned} \tag{41}$$

Using the trigonometric identity (A5)

$$\sin\left(\pi\ \frac{(j_1+1)k_1}{N_1}\right)-\sin\left(\pi\ \frac{j_1k_1}{N_1}\right)=2\sin\left(\frac{\pi}{2}\ \frac{k_1}{N_1}\right)\cos\left(\pi\ \frac{(j_1+\frac{1}{2})k_1}{N_1}\right) \tag{42}$$

we are thus led to the formula

$$H^{xx}[\mathbf{j}]=\sum_{k_1=1}^{N_1-1}\sum_{k_2=1}^{N_2-2}\sum_{k_3=1}^{N_3-2}\frac{2}{h_1}\sin\left(\frac{\pi}{2}\ \frac{k_1}{N_1}\right)\hat{u}[\mathbf{k}]\cos\left(\pi\ \frac{(j_1+\frac{1}{2})k_1}{N_1}\right)\sin\left(\pi\ \frac{j_2k_2}{N_2-1}\right)\sin\left(\pi\ \frac{j_3k_3}{N_3-1}\right) \tag{43}$$

The displacement gradient (16) may be computed from the sine coefficients (38) of the field u by a modulation of the coefficients and a `DCT-III` transform in x-direction and `DST-I` transforms in both the y- and the z-direction.

Similar expressions may be obtained for the displacement-gradient component (17)

$$H^{yy}[\mathbf{j}]=\sum_{k_1=1}^{N_1-2}\sum_{k_2=1}^{N_2-1}\sum_{k_3=1}^{N_3-2}\frac{2}{h_2}\sin\left(\frac{\pi}{2}\ \frac{k_2}{N_2}\right)\hat{v}[\mathbf{k}]\sin\left(\pi\ \frac{j_1k_1}{N_1-1}\right)\cos\left(\pi\ \frac{(j_2+\frac{1}{2})k_2}{N_2}\right)\sin\left(\pi\ \frac{j_3k_3}{N_3-1}\right) \tag{44}$$

and the displacement-gradient component (18)

$$H^{zz}[\mathbf{j}]=\sum_{k_1=1}^{N_1-2}\sum_{k_2=1}^{N_2-2}\sum_{k_3=1}^{N_3-1}\frac{2}{h_3}\sin\left(\frac{\pi}{2}\ \frac{k_3}{N_3}\right)\hat{w}[\mathbf{k}]\sin\left(\pi\ \frac{j_1k_1}{N_1-1}\right)\sin\left(\pi\ \frac{j_2k_2}{N_2-1}\right)\cos\left(\pi\ \frac{(j_3+\frac{1}{2})k_3}{N_3}\right) \tag{45}$$

The off-diagonal components of the displacement gradient may be determined with a similar logic. For instance, we obtain for the H^{xy}-gradient (20), written in the form

$$h_2\ H^{xy}[\mathbf{j}]=u[\mathbf{j}]-u[\mathbf{j}-\boldsymbol{e}_2] \tag{46}$$

the formula

$$h_2\ H^{xy}[\mathbf{j}]=\sum_{k_1=1}^{N_1-1}\sum_{k_2=1}^{N_2-2}\sum_{k_3=1}^{N_3-2}\hat{u}[\mathbf{k}]\sin\left(\pi\ \frac{j_1k_1}{N_1}\right)\left[\sin\left(\pi\ \frac{j_2k_2}{N_2-1}\right)-\sin\left(\pi\ \frac{(j_2-1)k_2}{N_2-1}\right)\right]\sin\left(\pi\ \frac{j_3k_3}{N_3-1}\right) \tag{47}$$

Taking into account the trigonometric identity (A7)

$$\sin\left(\pi\ \frac{j_2k_2}{N_2-1}\right)-\sin\left(\pi\ \frac{(j_2-1)k_2}{N_2-1}\right)=2\ \cos\left(\pi\ \frac{\left(j_2-\frac{1}{2}\right)k_2}{N_2-1}\right)\sin\frac{\pi k_2}{2(N_2-1)} \tag{48}$$

we are led to the formula

$$H^{xy}[\mathbf{j}]=\sum_{k_1=1}^{N_1-1}\sum_{k_2=1}^{N_2-2}\sum_{k_3=1}^{N_3-2}\frac{2}{h_2}\ \sin\frac{\pi k_2}{2(N_2-1)}\hat{u}[\mathbf{k}]\sin\left(\pi\ \frac{j_1k_1}{N_1}\right)\cos\left(\pi\ \frac{\left(j_2-\frac{1}{2}\right)k_2}{N_2-1}\right)\sin\left(\pi\ \frac{j_3k_3}{N_3-1}\right) \tag{49}$$

Similar arguments yield expressions for the other shear components of the tensor $\boldsymbol{H}$

$$H^{yx}[\mathbf{j}]=\sum_{k_1=1}^{N_1-2}\sum_{k_2=1}^{N_2-1}\sum_{k_3=1}^{N_3-2}\frac{2}{h_1}\ \sin\frac{\pi k_1}{2(N_1-1)}\hat{v}[\mathbf{k}]\cos\left(\pi\ \frac{\left(j_1-\frac{1}{2}\right)k_1}{N_1-1}\right)\sin\left(\pi\ \frac{j_2k_2}{N_2}\right)\sin\left(\pi\ \frac{j_3k_3}{N_3-1}\right) \tag{50}$$

$$H^{xz}[\mathbf{j}]=\sum_{k_1=1}^{N_1-1}\sum_{k_2=1}^{N_2-2}\sum_{k_3=1}^{N_3-2}\frac{2}{h_3}\ \sin\frac{\pi k_3}{2(N_3-1)}\hat{u}[\mathbf{k}]\sin\left(\pi\ \frac{j_1k_1}{N_1}\right)\sin\left(\pi\ \frac{j_2k_2}{N_2-1}\right)\cos\left(\pi\ \frac{\left(j_3-\frac{1}{2}\right)k_3}{N_3-1}\right) \tag{51}$$

$$H^{zx}[\mathbf{j}] = \sum_{k_1=1}^{N_1-2N_2-2N_3-1} \sum_{k_2=1} \sum_{k_3=1} \frac{2}{h_1} \sin \frac{\pi k_1}{2(N_1-1)} \hat{w}[\mathbf{k}] \cos\left(\pi \frac{\left(j_1-\frac{1}{2}\right)k_1}{N_1-1}\right) \sin\left(\pi \frac{j_2 k_2}{N_2-1}\right) \sin\left(\pi \frac{j_3 k_3}{N_3}\right) \tag{52}$$

$$H^{yz}[\mathbf{j}] = \sum_{k_1=1}^{N_1-2N_2-1N_3-2} \sum_{k_2=1} \sum_{k_3=1} \frac{2}{h_3} \sin \frac{\pi k_3}{2(N_3-1)} \hat{v}[\mathbf{k}] \sin\left(\pi \frac{j_1 k_1}{N_1-1}\right) \sin\left(\pi \frac{j_2 k_2}{N_2}\right) \cos\left(\pi \frac{\left(j_3-\frac{1}{2}\right)k_3}{N_3-1}\right) \tag{53}$$

$$H^{zy}[\mathbf{j}] = \sum_{k_1=1}^{N_1-2N_2-2N_3-1} \sum_{k_2=1} \sum_{k_3=1} \frac{2}{h_2} \sin \frac{\pi k_2}{2(N_2-2)} \hat{w}[\mathbf{k}] \sin\left(\pi \frac{j_1 k_1}{N_1-1}\right) \cos\left(\pi \frac{\left(j_2-\frac{1}{2}\right)k_2}{N_2-1}\right) \sin\left(\pi \frac{j_3 k_3}{N_3}\right) \tag{54}$$

Dual to formulas for the displacement gradient, we wish to develop expressions for the divergence operator (34–36) applied to a tensor field. For this purpose, we develop the components of a (potentially non-symmetric) stress field $\boldsymbol{P}$ into suitable series—compatible to the expressions for the displacement gradient—as follows:

$$P^{xx}[\mathbf{j}] = \sum_{k_1=1}^{N_1-1N_2-2N_3-2} \sum_{k_2=1} \sum_{k_3=1} \hat{P}^{xx}[\mathbf{k}] \cos\left(\pi \frac{(j_1+\frac{1}{2})k_1}{N_1}\right) \sin\left(\pi \frac{j_2 k_2}{N_2-1}\right) \sin\left(\pi \frac{j_3 k_3}{N_3-1}\right) \tag{55}$$

$$P^{xy}[\mathbf{j}] = \sum_{k_1=1}^{N_1-1N_2-2N_3-2} \sum_{k_2=1} \sum_{k_3=1} \hat{P}^{xy}[\mathbf{k}] \sin\left(\pi \frac{j_1 k_1}{N_1}\right) \cos\left(\pi \frac{\left(j_2-\frac{1}{2}\right)k_2}{N_2-1}\right) \sin\left(\pi \frac{j_3 k_3}{N_3-1}\right) \tag{56}$$

$$P^{xz}[\mathbf{j}] = \sum_{k_1=1}^{N_1-1N_2-2N_3-2} \sum_{k_2=1} \sum_{k_3=1} \hat{P}^{xz}[\mathbf{k}] \sin\left(\pi \frac{j_1 k_1}{N_1}\right) \sin\left(\pi \frac{j_2 k_2}{N_2-1}\right) \cos\left(\pi \frac{\left(j_3-\frac{1}{2}\right)k_3}{N_3-1}\right) \tag{57}$$

$$P^{yx}[\mathbf{j}] = \sum_{k_1=1}^{N_1-2N_2-1N_3-2} \sum_{k_2=1} \sum_{k_3=1} \hat{P}^{yx}[\mathbf{k}] \cos\left(\pi \frac{\left(j_1-\frac{1}{2}\right)k_1}{N_1-1}\right) \sin\left(\pi \frac{j_2 k_2}{N_2}\right) \sin\left(\pi \frac{j_3 k_3}{N_3-1}\right) \tag{58}$$

$$P^{yy}[\mathbf{j}] = \sum_{k_1=1}^{N_1-2N_2-1N_3-2} \sum_{k_2=1} \sum_{k_3=1} \hat{P}^{yy}[\mathbf{k}] \sin\left(\pi \frac{j_1 k_1}{N_1-1}\right) \cos\left(\pi \frac{(j_2+\frac{1}{2})k_2}{N_2}\right) \sin\left(\pi \frac{j_3 k_3}{N_3-1}\right) \tag{59}$$

$$P^{yz}[\mathbf{j}] = \sum_{k_1=1}^{N_1-2N_2-1N_3-2} \sum_{k_2=1} \sum_{k_3=1} \hat{P}^{yz}[\mathbf{k}] \sin\left(\pi \frac{j_1 k_1}{N_1-1}\right) \sin\left(\pi \frac{j_2 k_2}{N_2}\right) \cos\left(\pi \frac{\left(j_3-\frac{1}{2}\right)k_3}{N_3-1}\right) \tag{60}$$

$$P^{zx}[\mathbf{j}] = \sum_{k_1=1}^{N_1-2N_2-2N_3-1} \sum_{k_2=1} \sum_{k_3=1} \hat{P}^{zx}[\mathbf{k}] \cos\left(\pi \frac{\left(j_1-\frac{1}{2}\right)k_1}{N_1-1}\right) \sin\left(\pi \frac{j_2 k_2}{N_2-1}\right) \sin\left(\pi \frac{j_3 k_3}{N_3}\right) \tag{61}$$

$$P^{zy}[\mathbf{j}] = \sum_{k_1=1}^{N_1-2N_2-2N_3-1} \sum_{k_2=1} \sum_{k_3=1} \hat{P}^{zy}[\mathbf{k}] \sin\left(\pi \frac{j_1 k_1}{N_1-1}\right) \cos\left(\pi \frac{\left(j_2-\frac{1}{2}\right)k_2}{N_2-1}\right) \sin\left(\pi \frac{j_3 k_3}{N_3}\right) \tag{62}$$

$$P^{zz}[\mathbf{j}] = \sum_{k_1=1}^{N_1-2N_2-2N_3-1} \sum_{k_2=1} \sum_{k_3=1} \hat{P}^{zz}[\mathbf{k}] \sin\left(\pi \frac{j_1 k_1}{N_1-1}\right) \sin\left(\pi \frac{j_2 k_2}{N_2-1}\right) \cos\left(\pi \frac{(j_3+\frac{1}{2})k_3}{N_3}\right) \tag{63}$$

Then, we may take a closer look at the divergence operator (34)

$$f^x[\mathbf{j}] = \frac{P^{xx}[\mathbf{j}] - P^{xx}[\mathbf{j}-\boldsymbol{e}_1]}{h_1} + \frac{P^{xy}[\mathbf{j}+\boldsymbol{e}_2] - P^{xy}[\mathbf{j}]}{h_2} + \frac{P^{xz}[\mathbf{j}+\boldsymbol{e}_3] - P^{xz}[\mathbf{j}]}{h_3} \tag{64}$$

For the first summand, we observe

$$P^{xx}[\mathbf{j}] - P^{xx}[\mathbf{j} - \boldsymbol{e}_1] = \sum_{k_1=1}^{N_1-1}\sum_{k_2=1}^{N_2-2}\sum_{k_3=1}^{N_3-2} \hat{P}^{xx}[\mathbf{k}]\left[\cos\left(\pi\,\frac{(j_1+\frac{1}{2})k_1}{N_1}\right) - \cos\left(\pi\,\frac{(j_1-\frac{1}{2})k_1}{N_1}\right)\right]\sin\left(\pi\,\frac{j_2k_2}{N_2-1}\right)\sin\left(\pi\,\frac{j_3k_3}{N_3-1}\right) \tag{65}$$

With the help of the trigonometric formula (A11), we obtain the result

$$\cos\left(\pi\,\frac{(j_1+\frac{1}{2})k_1}{N_1}\right) - \cos\left(\pi\,\frac{(j_1-\frac{1}{2})k_1}{N_1}\right) = -2\sin\left(\pi\,\frac{j_1k_1}{N_1}\right)\sin\frac{\pi\,k_1}{2N_1} \tag{66}$$

which we may reinsert into the expression (34) to obtain the formula

$$\frac{P^{xx}[\mathbf{j}] - P^{xx}[\mathbf{j} - \boldsymbol{e}_1]}{h_1} = -\sum_{k_1=1}^{N_1-1}\sum_{k_2=1}^{N_2-2}\sum_{k_3=1}^{N_3-2}\frac{2}{h_1}\sin\frac{\pi\,k_1}{2N_1}\hat{P}^{xx}[\mathbf{k}]\sin\left(\pi\,\frac{j_1k_1}{N_1}\right)\sin\left(\pi\,\frac{j_2k_2}{N_2-1}\right)\sin\left(\pi\,\frac{j_3k_3}{N_3-1}\right) \tag{67}$$

Similar arguments yield the expressions

$$\frac{P^{xy}[\mathbf{j} + \boldsymbol{e}_2] - P^{xy}[\mathbf{j}]}{h_2} = -\sum_{k_1=1}^{N_1-1}\sum_{k_2=1}^{N_2-2}\sum_{k_3=1}^{N_3-2}\frac{2}{h_2}\sin\frac{\pi\,k_2}{2(N_2-1)}\hat{P}^{xy}[\mathbf{k}]\sin\left(\pi\,\frac{j_1k_1}{N_1}\right)\sin\left(\pi\,\frac{j_2k_2}{N_2-1}\right)\sin\left(\pi\,\frac{j_3k_3}{N_3-1}\right) \tag{68}$$

and

$$\frac{P^{xz}[\mathbf{j} + \boldsymbol{e}_3] - P^{xz}[\mathbf{j}]}{h_3} = -\sum_{k_1=1}^{N_1-1}\sum_{k_2=1}^{N_2-2}\sum_{k_3=1}^{N_3-2}\frac{2}{h_3}\sin\frac{\pi\,k_3}{2(N_3-1)}\hat{P}^{xz}[\mathbf{k}]\sin\left(\pi\,\frac{j_1k_1}{N_1}\right)\sin\left(\pi\,\frac{j_2k_2}{N_2-1}\right)\sin\left(\pi\,\frac{j_3k_3}{N_3-1}\right) \tag{69}$$

Equivalent manipulations may be performed for the other components of the force field (34–36). Eventually, we end up with the following expressions

$$\hat{f}^x[\mathbf{k}] = -\left(\frac{2}{h_1}\sin\frac{\pi\,k_1}{2N_1}\hat{P}^{xx}[\mathbf{k}] + \frac{2}{h_2}\sin\frac{\pi\,k_2}{2(N_2-1)}\hat{P}^{xy}[\mathbf{k}] + \frac{2}{h_3}\sin\frac{\pi\,k_3}{2(N_3-1)}\hat{P}^{xz}[\mathbf{k}]\right) \tag{70}$$

$$\hat{f}^y[\mathbf{k}] = -\left(\frac{2}{h_1}\sin\frac{\pi\,k_1}{2(N_1-1)}\hat{P}^{yx}[\mathbf{k}] + \frac{2}{h_2}\sin\frac{\pi\,k_2}{2N_2}\hat{P}^{yy}[\mathbf{k}] + \frac{2}{h_3}\sin\frac{\pi\,k_3}{2(N_3-1)}\hat{P}^{yz}[\mathbf{k}]\right) \tag{71}$$

$$\hat{f}^z[\mathbf{k}] = -\left(\frac{2}{h_1}\sin\frac{\pi\,k_1}{2(N_1-1)}\hat{P}^{zx}[\mathbf{k}] + \frac{2}{h_2}\sin\frac{\pi\,k_2}{2(N_2-1)}\hat{P}^{zy}[\mathbf{k}] + \frac{2}{h_3}\sin\frac{\pi\,k_3}{2N_3}\hat{P}^{xz}[\mathbf{k}]\right) \tag{72}$$

for the sine coefficients of the force-vector field

$$f^x[\mathbf{j}] = \sum_{k_1=1}^{N_1-1}\sum_{k_2=1}^{N_2-2}\sum_{k_3=1}^{N_3-2}\hat{f}^x[\mathbf{k}]\sin\left(\pi\,\frac{j_1k_1}{N_1}\right)\sin\left(\pi\,\frac{j_2k_2}{N_2-1}\right)\sin\left(\pi\,\frac{j_3k_3}{N_3-1}\right) \tag{73}$$

$$f^y[\mathbf{j}] = \sum_{k_1=1}^{N_1-2}\sum_{k_2=1}^{N_2-1}\sum_{k_3=1}^{N_3-2}\hat{f}^y[\mathbf{k}]\sin\left(\pi\,\frac{j_1k_1}{N_1-1}\right)\sin\left(\pi\,\frac{j_2k_2}{N_2}\right)\sin\left(\pi\,\frac{j_3k_3}{N_3-1}\right) \tag{74}$$

$$f^z[\mathbf{j}] = \sum_{k_1=1}^{N_1-2}\sum_{k_2=1}^{N_2-2}\sum_{k_3=1}^{N_3-1}\hat{f}^z[\mathbf{k}]\sin\left(\pi\,\frac{j_1k_1}{N_1-1}\right)\sin\left(\pi\,\frac{j_2k_2}{N_2-1}\right)\sin\left(\pi\,\frac{j_3k_3}{N_3}\right) \tag{75}$$

which has the same form as the displacement fields (38–40).

2.4 | Green's Operator With Discrete Sine and Cosine Transforms

We wish to obtain an explicit formula for Green's operator (8) in our context. We follow our previous work [73] and use the reference "material" (6)

$$\boldsymbol{P} = \alpha_0 \, \boldsymbol{H} \tag{76}$$

for a positive constant α_0 with the dimensions of a stress.

We first take a look at the x-component of the force field vector (70). Inserting the relation from Equation (76) as well as the expressions (43–54) for the displacement gradient, we obtain the formula

$$\begin{aligned}
\hat{f}^x[\mathbf{k}] &= -\left(\frac{2}{h_1} \sin \frac{\pi \, k_1}{2N_1} \hat{P}^{xx}[\mathbf{k}] + \frac{2}{h_2} \sin \frac{\pi \, k_2}{2(N_2-1)} \hat{P}^{xy}[\mathbf{k}] + \frac{2}{h_3} \sin \frac{\pi \, k_3}{2(N_3-1)} \hat{P}^{xz}[\mathbf{k}] \right) \\
&= -\alpha_0 \left(\frac{2}{h_1} \sin \frac{\pi \, k_1}{2N_1} \hat{H}^{xx}[\mathbf{k}] + \frac{2}{h_2} \sin \frac{\pi \, k_2}{2(N_2-1)} \hat{H}^{xy}[\mathbf{k}] + \frac{2}{h_3} \sin \frac{\pi \, k_3}{2(N_3-1)} \hat{H}^{xz}[\mathbf{k}] \right) \\
&= -4\alpha_0 \left(\frac{1}{h_1^2} \sin^2 \frac{\pi \, k_1}{2N_1} + \frac{1}{h_2^2} \sin^2 \frac{\pi \, k_2}{2(N_2-1)} + \frac{1}{h_3^2} \sin^2 \frac{\pi \, k_3}{2(N_3-1)} \right) \hat{u}[\mathbf{k}]
\end{aligned} \tag{77}$$

Likewise, we obtain expressions for the remaining two components of the body-force field

$$\hat{f}^y[\mathbf{k}] = -4\alpha_0 \left(\frac{1}{h_1^2} \sin^2 \frac{\pi \, k_1}{2(N_1-1)} + \frac{1}{h_2^2} \sin^2 \frac{\pi \, k_2}{2N_2} + \frac{1}{h_3^2} \sin^2 \frac{\pi \, k_3}{2(N_3-1)} \right) \hat{v}[\mathbf{k}] \tag{78}$$

$$\hat{f}^z[\mathbf{k}] = -4\alpha_0 \left(\frac{1}{h_1^2} \sin^2 \frac{\pi \, k_1}{2(N_1-1)} + \frac{1}{h_2^2} \sin^2 \frac{\pi \, k_2}{2(N_2-1)} + \frac{1}{h_3^2} \sin^2 \frac{\pi \, k_3}{2N_3} \right) \hat{w}[\mathbf{k}] \tag{79}$$

In particular, Green's operator (7) computes as

$$\hat{u}[\mathbf{k}] = -\frac{\hat{f}^x[\mathbf{k}]}{4\alpha_0 \left(\frac{1}{h_1^2} \sin^2 \frac{\pi \, k_1}{2N_1} + \frac{1}{h_2^2} \sin^2 \frac{\pi \, k_2}{2(N_2-1)} + \frac{1}{h_3^2} \sin^2 \frac{\pi \, k_3}{2(N_3-1)} \right)} \tag{80}$$

$$\hat{v}[\mathbf{k}] = -\frac{\hat{f}^y[\mathbf{k}]}{4\alpha_0 \left(\frac{1}{h_1^2} \sin^2 \frac{\pi \, k_1}{2(N_1-1)} + \frac{1}{h_2^2} \sin^2 \frac{\pi \, k_2}{2N_2} + \frac{1}{h_3^2} \sin^2 \frac{\pi \, k_3}{2(N_3-1)} \right)} \tag{81}$$

$$\hat{w}[\mathbf{k}] = -\frac{\hat{f}^z[\mathbf{k}]}{4\alpha_0 \left(\frac{1}{h_1^2} \sin^2 \frac{\pi \, k_1}{2(N_1-1)} + \frac{1}{h_2^2} \sin^2 \frac{\pi \, k_2}{2(N_2-1)} + \frac{1}{h_3^2} \sin^2 \frac{\pi \, k_3}{2N_3} \right)} \tag{82}$$

at the frequencies $\mathbf{k}$ required by the inverse transforms (43–54). Finally, the Eshelby-Green operator (9) results from a sequential Fourier-space application of the divergence (64), then Green's operator (80–82) and finally the gradient (18–43).

3 | Implementation

3.1 | Introduction

FFT-based solvers in mechanics are usually implemented either on the displacement directly or on the (symmetric) displacement gradient. The displacement-based iteration scheme reduces the number of Fourier transforms that need to be evaluated but necessitates computing gradients by finite differences in real space [73]. Evaluating such finite difference stencils comes with a computational overhead because the relevant components are typically not located in close regions of memory, and computing the gradient in Fourier space is actually more efficient. For this reason and for compatibility

with conventional implementations, we implement a *displacement gradient*-based iteration scheme. To this end, we need to compute the Eshelby-Green operator (9)

$$\boldsymbol{\Gamma}_0 = \nabla \boldsymbol{G}_0 \mathrm{div} \tag{83}$$

in Fourier space where $\boldsymbol{G}_0$ refers to Green's operator (7). Applying the Eshelby-Green operator $\boldsymbol{\Gamma}_0$ in Fourier space, in conjunction with Dirichlet boundary conditions, necessitates computing transforms (16–25) utilizing predefined transforms from the selected FFT library [78].

3.2 | A Staggered Grid Solver With Dirichlet Boundary Conditions

To highlight the challenge at hand, we discuss a one-dimensional problem first. Based on the one-dimensional case, we assemble the three-dimensional case due to the inherent tensor product structure of the problem. In line with the logic of Section 2.3, we start with the transform of the displacement gradient $\boldsymbol{H}$. We perform a forward transform on the stress field $\boldsymbol{P}$ but perform a backward transform on the displacement gradient field $\hat{\boldsymbol{H}}$. Per the derivation (16–25), the shear components $H^{xy}[j_1, j_2, j_3]$ along the y-axis with fixed indices j_1 and j_3, are computed via the discrete cosine transform

$$H^{xy}[j_2] = \sum_{k=1}^{N-2} \hat{H}^{xy}[k] \cos\left(\pi \frac{\left(j_2 - \frac{1}{2}\right)k}{N-1}\right), \quad j_2 = 1, 2, \dots, N-1 \tag{84}$$

where we abuse notation and conceal the dependence on the indices j_1 and j_3 for the time being.

Using the FFTW library [78], we compute this transform using the `DST-III`. For an input signal

$$\hat{X} = (\hat{X}[0], \hat{X}[1], \dots, \hat{X}[M-1]) \in \mathbb{R}^M \tag{85}$$

the `DST-III` computes an output signal $X \in \mathbb{R}^M$ with components

$$X[\ell] = \hat{X}[0] + 2 \sum_{c=1}^{M-1} \hat{X}[c] \cos\left(\pi \frac{(\ell + \frac{1}{2})c}{M}\right), \quad \ell = 0, 1, \dots, M-1 \tag{86}$$

To compute the transform (84) using the `DCT-III`, we select the parameters $\ell = j_2 - 1$, $c = k$ as well as $M = N - 1$ and obtain

$$H^{xy}[j_2] = \frac{1}{2}\hat{H}^{xy}[1] + \sum_{c=1}^{N-2} \hat{H}^{xy}[c+1] \cos\left(\pi \frac{\left(j - \frac{1}{2}\right)c}{N-1}\right), \quad j_2 = 1, 2, \dots, N-1 \tag{87}$$

with $\hat{H}^{xy}[1] = 0$ to enforce a zero mean. By this definition, we obtain the components

$$H^{xy}[1], H^{xy}[2], \dots, H^{xy}[N-1] \tag{88}$$

and require the Fourier coefficients

$$\hat{H}^{xy}[1], \hat{H}^{xy}[2], \dots, \hat{H}^{xy}[N-2] \tag{89}$$

The forward transform of the stress field $\boldsymbol{P}$ (56) on the y-axis from real space to Fourier space is based on the `DCT-II` which, for an input signal $Z \in \mathbb{R}^K$ is defined [78] as

$$\hat{Z}[\xi] = 2 \sum_{\zeta=0}^{K-1} Z[\zeta] \cos\left(\frac{\pi\left(\zeta + \frac{1}{2}\right)\xi}{K}\right), \quad \xi = 0, 1, \dots, K-1 \tag{90}$$

By choosing the parameters $j = \zeta + 1$, $K = N - 1$ and after a coordinate shift we obtain

$$\hat{P}^{xy}[\xi + 1] = 2 \sum_{j=1}^{N-1} P^{xy}[j_2] \cos\left(\frac{\pi\left(j_2 - \frac{1}{2}\right)\xi}{N-1} \right), \quad \xi = 0, 1, \dots N - 2 \tag{91}$$

providing the Fourier coefficients $\hat{P}^{xy}[1], \hat{P}^{xy}[2], \dots, \hat{P}^{xy}[N-1]$ required for the inverse transform.

Turning our attention to the z-direction perpendicular to the derivative $H^{xy}[j_1, j_2, j_3]$, that is, for an index $j = j_3$ and fixed indices j_1 as well as j_2, we have

$$H^{xy}[j_3] = \sum_{k=1}^{N-2} \hat{H}^{xy}[k] \sin\left(\pi \frac{j_3 k}{N-1} \right) \tag{92}$$

The `DST-I` is defined as follows

$$X[\ell] = 2 \sum_{c=0}^{M-1} \hat{X}[c] \sin\left(\pi \frac{(\ell + 1)(c+1)}{M+1} \right), \quad \ell = 0, 1, \dots, M - 1 \tag{93}$$

With the substitutions $j = \ell + 1$, $N = M + 2$, we have the equivalent transform

$$X[j_3 - 1] = 2 \sum_{c=0}^{N-3} \hat{X}[c] \sin\left(\pi \frac{j_3 (c+1)}{N-1} \right) \quad j_3 = 1, 2, \dots, N - 2 \tag{94}$$

which yields the displacement gradient component

$$H^{xy}[j_3] = 2 \sum_{k=1}^{N-2} \hat{H}^{xy}[k] \sin\left(\pi \frac{j_3 k}{N-1} \right) \quad j_3 = 1, 2, \dots, N - 2 \tag{95}$$

Similar strategies permit to represent all forward transforms of the components of the stress $\boldsymbol{P}$ (63) which are listed in Table 1 as well as the backward transforms all other components of the field $\hat{\boldsymbol{H}}$ (18–43) which are listed in Table 2.

After deriving the necessary discrete sine and cosine transforms in Section 2 and clarifying the transfer of those transforms to the FFTW library in a one-dimensional case, we turn our focus to the actual implementation of the homogenization for three-dimensional problems. The basic scheme (12) is discussed in Algorithm 1. We show the basic scheme for exposure, but the same Eshelby-Green operator (9) can likewise be used for faster solver methods like linear CG [74].

TABLE 1 | Details for the discrete sine and cosine transforms to enforce Dirichlet boundary conditions for the staggered grid discretization to compute the transformed components of the stress field $\hat{\boldsymbol{P}}$.

	***x*-axis**			***y*-axis**			***z*-axis**			
	DFT	$j_{\min}$	$j_{\max}$	**DFT**	$j_{\min}$	$j_{\max}$	**DFT**	$j_{\min}$	$j_{\max}$	**Shift**
P^{xx}	`DCT-II`	0	$N_x - 1$	`DST-I`	1	$N_y - 2$	`DST-I`	1	$N_z - 2$	—
P^{xy}	`DST-I`	1	$N_x - 1$	`DCT-II`	1	$N_y - 1$	`DST-I`	1	$N_z - 2$	y
P^{xz}	`DST-I`	1	$N_x - 1$	`DST-I`	1	$N_y - 2$	`DCT-II`	1	$N_z - 1$	z
P^{yx}	`DCT-II`	1	$N_x - 1$	`DST-I`	1	$N_y - 1$	`DST-I`	1	$N_z - 2$	x
P^{yy}	`DST-I`	1	$N_x - 2$	`DCT-II`	0	$N_y - 1$	`DST-I`	1	$N_z - 2$	—
P^{yz}	`DST-I`	1	$N_x - 2$	`DST-I`	1	$N_y - 1$	`DCT-II`	1	$N_z - 1$	z
P^{zx}	`DCT-II`	1	$N_x - 1$	`DST-I`	1	$N_y - 2$	`DST-I`	1	$N_z - 1$	x
P^{zy}	`DST-I`	1	$N_x - 2$	`DCT-II`	1	$N_y - 1$	`DST-I`	1	$N_z - 1$	y
P^{zz}	`DST-I`	1	$N_x - 2$	`DST-I`	1	$N_y - 2$	`DCT-II`	0	$N_z - 1$	—

TABLE 2 | Details for the *inverse* discrete sine and cosine transforms to enforce Dirichlet boundary conditions for the staggered grid discretization to compute the transformed components of the displacement gradient field $\boldsymbol{H}$.

	x-axis			y-axis			z-axis			shift	
	DFT	$k_{\min}$	$k_{\max}$	**DFT**	$k_{\min}$	$k_{\max}$	**DFT**	$k_{\min}$	$k_{\max}$	**axis**	**Normalization b**
$\hat{H}^{xx}$	DCT-III	0	$N_x - 1$	DST-I	1	$N_y - 2$	DST-I	1	$N_z - 2$	—	$N_x(N_y-1)(N_z-1)$
$\hat{H}^{xy}$	DST-I	1	$N_x - 1$	DCT-III	1	$N_y - 1$	DST-I	1	$N_z - 2$	y	$N_x(N_y-1)(N_z-1)$
$\hat{H}^{xz}$	DST-I	1	$N_x - 1$	DST-I	1	$N_y - 2$	DCT-III	1	$N_z - 1$	z	$N_x(N_y-1)(N_z-1)$
$\hat{H}^{yx}$	DCT-III	1	$N_x - 1$	DST-I	1	$N_y - 1$	DST-I	1	$N_z - 2$	x	$(N_x-1)N_y(N_z-1)$
$\hat{H}^{yy}$	DST-I	1	$N_x - 2$	DCT-III	0	$N_y - 1$	DST-I	1	$N_z - 2$	—	$(N_x-1)N_y(N_z-1)$
$\hat{H}^{yz}$	DST-I	1	$N_x - 2$	DST-I	1	$N_y - 1$	DCT-III	1	$N_z - 1$	z	$(N_x-1)N_y(N_z-1)$
$\hat{H}^{zx}$	DCT-III	1	$N_x - 1$	DST-I	1	$N_y - 2$	DST-I	1	$N_z - 1$	x	$(N_x-1)(N_y-1)N_z$
$\hat{H}^{zy}$	DST-I	1	$N_x - 2$	DCT-III	1	$N_y - 1$	DST-I	1	$N_z - 1$	y	$(N_x-1)(N_y-1)N_z$
$\hat{H}^{zz}$	DST-I	1	$N_x - 2$	DST-I	1	$N_y - 2$	DCT-III	0	$N_z - 1$	—	$(N_x-1)(N_y-1)N_z$

ALGORITHM 1 | Basic scheme with prescribed strain on the staggered grid.

1: $\boldsymbol{H} \leftarrow \bar{\boldsymbol{\varepsilon}}$
2: $\mathtt{res} \leftarrow \mathtt{tol} + 1$
3: **while** $\mathtt{res} \geq \mathtt{tol}$ **do**
4: $\quad \boldsymbol{H}_{\text{old}} \leftarrow \boldsymbol{H}$
5: $\quad \boldsymbol{P} \leftarrow \mathbb{C} : \boldsymbol{H} - \alpha_0 \boldsymbol{H}$
6: $\quad \bar{\boldsymbol{\sigma}} \leftarrow \mathtt{mean}(\boldsymbol{P}) + \alpha_0 \bar{\boldsymbol{\varepsilon}}$
7: $\quad \boldsymbol{H} \leftarrow \mathtt{apply\_Gamma0}(\boldsymbol{P})$ ▷ Algorithm 2
8: $\quad \boldsymbol{H} \leftarrow \bar{\boldsymbol{\varepsilon}} + \boldsymbol{H}$
9: $\quad \mathtt{res} \leftarrow \frac{\alpha_0 \left\| \boldsymbol{H} - \boldsymbol{H}_{\text{old}} \right\|}{\|\bar{\boldsymbol{\sigma}}\|}$
10: $\quad$ **return** $\boldsymbol{H}, \bar{\boldsymbol{\sigma}}$
11: **end while**

For periodic boundary conditions, the mean of the field may be prescribed by adjusting the zeroth Fourier coefficient appropriately [52]. Matters are not so simple for Dirichlet boundary conditions and discrete sine/cosine transforms. The zero frequency is not inherently related to the mean of a field consisting of a mix of the discrete cosine and sine transforms, but only to the mean on the axis of the discrete cosine transform. Therefore, we compute the means as a conventional sum over the whole field, taking into account the unequal reduced sizes of the axes due to the boundary conditions. The same obstacle holds for setting the mean of a field, which is a crucial part of the basic scheme in Algorithm 1, l. 6, to enforce the macroscopic boundary condition.

Please note that the domain of the DSTs listed in Table 1 operates on a subset of the full set of boundary nodes only. The remaining nodes must be set to zero separately. Therefore, after the transformation back to real space as listed in Table 2, we manually set the remaining boundary values to zero.

Details for applying the Eshelby-Green operator are contained in Algorithm 2. In contrast to the periodic case, two different vectors $\boldsymbol{\xi}$ and $\boldsymbol{\zeta}$—with three components each—need to be precomputed, where the periodic case only requires half the number of components [32].

The FFTW library works best in place [78]. Therefore, we shift the transformed field to obtain the coefficients in the correct locations with the indices starting from zero for all components. Nevertheless, to select the correct indices $\mathbf{k}$ in Algorithm 1, a shift allows us to use the listed entries. The shift is only necessary on a single axis per transform on the off-diagonal components of the field. The shifted axis is listed in Table 1 for the backwards shift performed after the forward transform and in Table 2 for the forward shift performed before the backward transform. Moreover, the FFTW library computes non-normalized transforms. Therefore, the normalization of the transformed components needs to be handled. The respective normalization factors applied after the backwards transform are listed in Table 2.

ALGORITHM 2 | `apply_Gamma0(`$\boldsymbol{P}$`)`.

Require: local stress field $\boldsymbol{P}$

1: $\hat{\boldsymbol{P}} \leftarrow$ `DFT(`$\boldsymbol{P}$`)` ▷ Forward transform, see Table 1

2: $\hat{\boldsymbol{P}} \leftarrow$ `shift_backward(`$\hat{\boldsymbol{P}}$`)`

3: **for** $\mathbf{k} \in \mathbb{N}_N^3$ **do**

4: $\quad \boldsymbol{\xi}(\mathbf{k}) \leftarrow \begin{bmatrix} 2N_1 \sin\left(\frac{\pi k_1}{2N_1}\right) \\ 2N_2 \sin\left(\frac{\pi k_2}{2N_2}\right) \\ 2N_3 \sin\left(\frac{\pi k_3}{2N_3}\right) \end{bmatrix}$ ▷ Precomputed diagonal factors

5: $\quad \boldsymbol{\zeta}(\mathbf{k}) \leftarrow \begin{bmatrix} 2N_1 \sin\left(\frac{\pi k_1}{2(N_1-1)}\right) \\ 2N_2 \sin\left(\frac{\pi k_2}{2(N_2-1)}\right) \\ 2N_3 \sin\left(\frac{\pi k_3}{2(N_3-1)}\right) \end{bmatrix}$ ▷ Precomputed off-diagonal factors

6: $\quad \boldsymbol{p} \leftarrow \begin{bmatrix} \alpha_0\left(\xi_1^2 + \zeta_2^2 + \zeta_3^2\right) \\ \alpha_0\left(\zeta_1^2 + \xi_2^2 + \zeta_3^2\right) \\ \alpha_0\left(\zeta_1^2 + \zeta_2^2 + \xi_3^2\right) \end{bmatrix}$

7: $\quad \hat{\boldsymbol{u}} \leftarrow \begin{bmatrix} \left(\xi_1 \hat{P}^{xx} + \zeta_2 \hat{P}^{xy} + \zeta_3 \hat{P}^{xz}\right)/p_x \\ \left(\zeta_1 \hat{P}^{yx} + \xi_2 \hat{P}^{yy} + \zeta_3 \hat{P}^{yz}\right)/p_y \\ \left(\zeta_1 \hat{P}^{zx} + \zeta_2 \hat{P}^{zy} + \xi_3 \hat{P}^{zz}\right)/p_z \end{bmatrix}$

8: $\quad \hat{\boldsymbol{H}} \leftarrow \begin{bmatrix} \xi_1 \hat{u}_1 & \zeta_2 \hat{u}_1 & \zeta_3 \hat{u}_1 \\ \zeta_1 \hat{u}_2 & \xi_2 \hat{u}_2 & \zeta_3 \hat{u}_2 \\ \zeta_1 \hat{u}_3 & \zeta_2 \hat{u}_2 & \xi_3 \hat{u}_3 \end{bmatrix}$

9: **end for**

10: $\hat{\boldsymbol{H}} \leftarrow$ `_forward(`$\hat{\boldsymbol{H}}$`)`

11: $\boldsymbol{H} \leftarrow$ `iDFT(`$\hat{\boldsymbol{H}}$`)` ▷ Backward transform transform, see Table 2

12: $\boldsymbol{H} \leftarrow \boldsymbol{H}/(8b)$ ▷ Normalization, see Table 2

13: **return** $\boldsymbol{H}$

The material law is evaluated in l. 5 of Algorithm 1. Generally, we want to restrict to a small strain setting. Nevertheless, we operate on large-strain displacement gradients as well as a corresponding non-symmetrized strain measure for compatibility with the discrete sine and cosine transforms necessary to apply the boundary conditions, as demonstrated in Section 2.3. The skew-symmetric part of the displacement gradient, which arises from numerical considerations rather than the fundamental problem setting, is, in fact, inconsequential as the material law is applied to the symmetrized displacement gradient only. This approach enables improved performance and re-usability of material law implementations. Following this strategy [73], we cast the symmetric stress components to the off-diagonal components of the large-strain stress tensor. As a result, the number of components in the material law at each node is reduced from nine to six. This reduction in complexity yields a notable improvement in computational efficiency. The staggered grid discretization allows for different, not necessarily consistent, methods of applying the material law. As with all voxel-based solution methods, a single material law is assigned to each voxel (composite voxel methods [79–81] notwithstanding). The application of the material law for the normal stress components and isotropic linear elastic material behavior is straightforward. For normal components, the material law is implemented using the material properties corresponding to the voxel in which the centroid of the normal components resides. The shear components, on the other hand, live on the edges between adjacent voxels. Therefore, it is not inherently clear which voxel's material law needs to be chosen for the shear components of each voxel. The naive, but established method is to consistently assign the material law of the voxel in the positive direction of the axes [32]. Alternatively, the material properties of the surrounding voxels may be mixed [82].

4 | Computational Investigations

4.1 | Setup

In this section, we investigate the numerical performance of the presented solution framework for the staggered grid discretization with Dirichlet boundary conditions. To this end, we thoroughly modified our in-house strain-based FFT

solver, comprising the inclusion of the transforms discussed in Section 3 using the FFTW library [78] as well as the modification of the Eshelby-Green operator detailed in Algorithm 2. All other building blocks, including the conjugate gradient (CG) solver, which we used for all following investigations, operate in a manner consistent with prior methods. Runtimes are measured on an AMD EPYC CPU with 64 cores and 1152 GB of RAM. The authors' prior work on the Moulinec-Suquet [72] and the Q1R [73] discretization with Dirichlet boundary conditions serves as a benchmark. In the following, we investigate the performance of FFT-based homogenization methods with Dirichlet boundary conditions on a staggered grid for a number of heterogeneous microstructure types. We start with a spherical inclusion with finite contrast, which does not pose a problem even for the Moulinec-Suquet discretization, and continue with a more challenging bicontinuous stochastic microstructured material, which also involves a finite material contrast. Subsequently, we turn our attention to a sand grain microstructure, which is characterized by an infinite contrast. Finally, we examine a polymer foam microstructure, which is characterized by an infinite material contrast and a low volume fraction of the solid material. This microstructure is particularly challenging for FFT-based homogenization problems.

4.2 | Spherical Inclusion – Finite Contrast

First, we investigate a spherical glass inclusion embedded in an epoxy matrix with linear elastic behavior for both phases. For the glass phase, we assume a Young's modulus $E = 72$ MPa and Poisson's ratio $\nu = 0.2$. We furnish the epoxy phase with a Young's modulus $E = 3.0$ MPa and Poisson's ratio $\nu = 0.35$. The spherical inclusion is resolved on a cubic domain $[0, L]^3$ with an edge length L and a spherical inclusion of radius $5/16L$. We compare the staggered grid discretization, introduced in Section 2.2 with vanishing Dirichlet data to the Moulinec-Suquet discretization [72] and to the Q1R discretization with Dirichlet boundary conditions [73].

Figure 3 shows a slice of the local stress fields for a spherical inclusion resolved on a 256^3 grid for a mean strain of 5% in x-direction. All three solution fields show a high degree of agreement in Figure 3. The zoomed view of the same field is shown in Figure 4. In Figure 4a, the Moulinec-Suquet discretization shows strong oscillations. In Figure 4b, the Q1R discretizations exhibit a strong checkerboarding effect, especially in the vicinity of the material interfaces. In contrast, in Figure 4c, we notice significantly fewer oscillations for the staggered grid discretization. For periodic boundary conditions [32], similar observations were made. Figure 5a shows the apparent mean stress for increasing voxel count. Notably, the apparent mean stress is higher for the staggered grid discretization and at a low resolution of 32^3. For higher resolutions, the staggered grid yields slightly lower apparent mean stresses than the Moulinec-Suquet or the Q1R discretizations. This slightly lower apparent stress was also observed for the case of periodic boundary conditions [52].

Figure 5b shows the convergence behavior of all three discretization schemes with Dirichlet boundary conditions. With a finite material contrast and linear elastic material behavior, the staggered grid discretization does not show a noticeable difference concerning the convergence of the solution scheme. In fact, the staggered grid needs 41 CG iterations to reach the desired tolerance 10^{-5}, whereas the residual falls below the tolerance in only 34 and 40 iterations for the Q1R and Moulinec-Suquet discretizations, respectively.

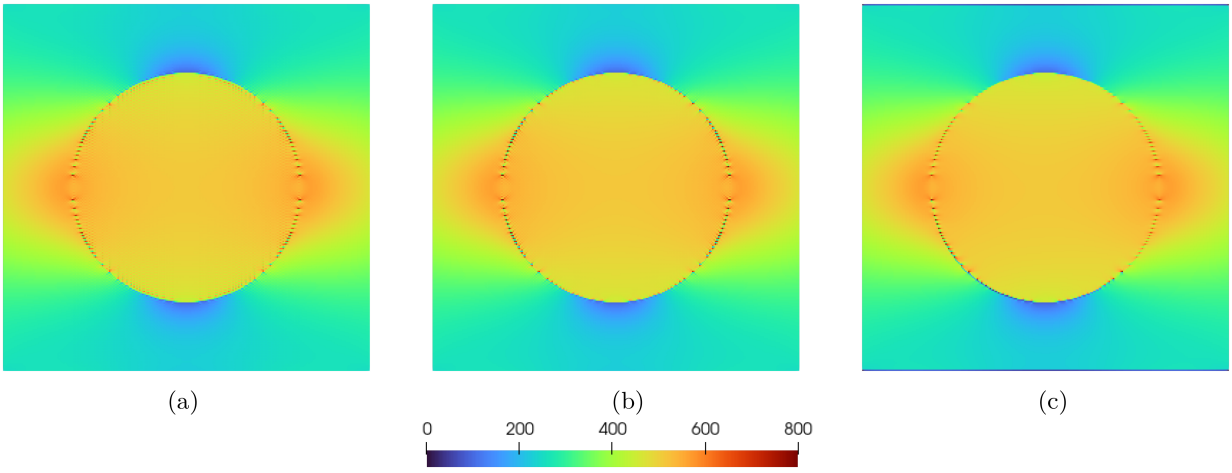

FIGURE 3 | Local stress field σ_{xx} in MPa for different discretizations with Dirichlet boundary conditions. (a) Moulinec-Suquet, (b) Q1R, and (c) staggered grid.

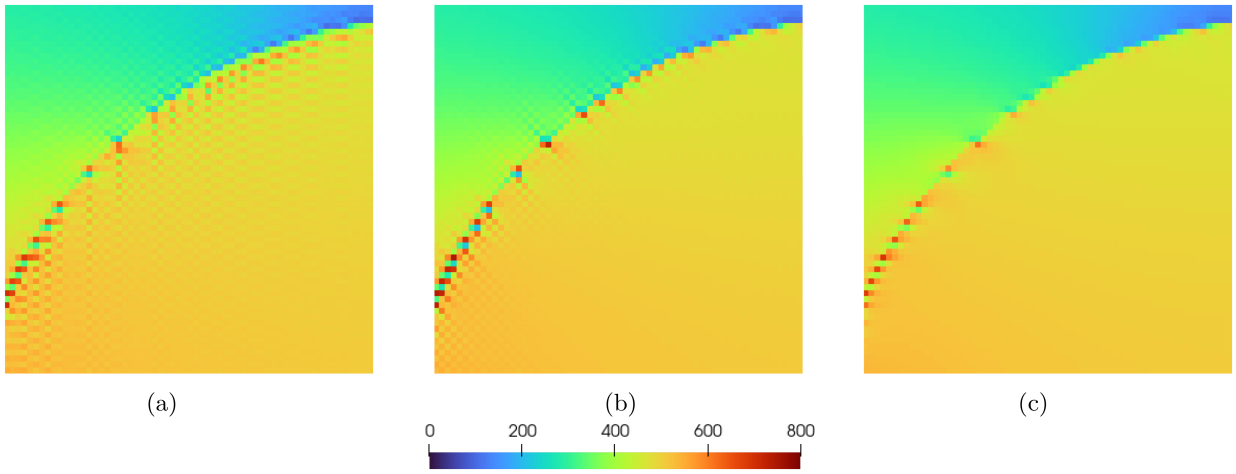

FIGURE 4 | Zoom of the local stress field σ_{xx} in MPa for different discretizations with Dirichlet boundary conditions. Note the absence of artifacts in the bulk for the staggered grid discretization. (a) Moulinec-Suquet, (b) Q1R, and (c) staggered grid.

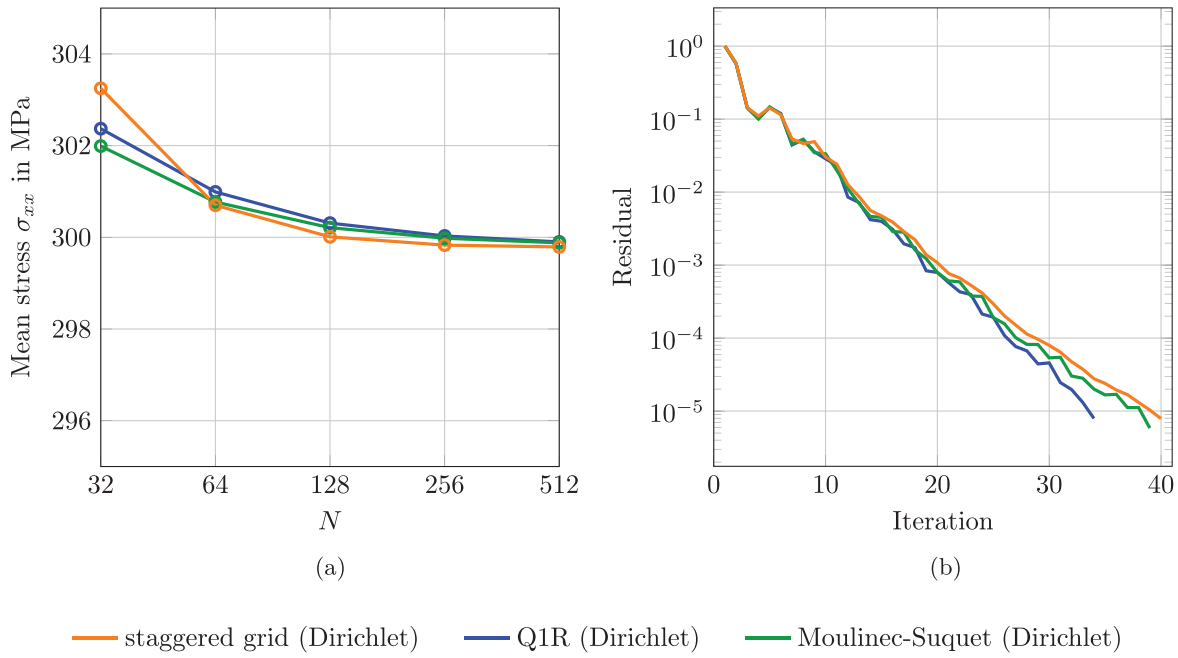

FIGURE 5 | Spherical glass inclusion in a polymer matrix with Dirichlet boundary conditions. (a) Mean stress σ_{xx} for increasing resolution, (b) residual versus iteration of the linear CG solver for 512^3 voxels.

4.3 | Bicontinuous Stochastic Composites – Finite Contrast

The process of phase separation of metal alloys is described by the Cahn-Hilliard equation [83–85]. An approximation of an intermediate state of this dealloying process is given by a Gaussian Random Field (GRF) [86, 87]. The microstructures generated as a level set decomposition of the GRF may describe bicontinuous stochastic composites such as epoxy-filled nanoporous gold [88–90] and serve as a basis for microstructures with properties optimized by inverse design [91, 92]. Figure 6 shows an example of such a bicontinuous stochastic microstructure.

Soyarslan et al. [93] investigated the effective mechanical properties of an epoxy-filled nanoporous gold composite using conventional FE methods, where the authors generated periodic bicontinuous stochastic microstructures of various sizes and computed their effective elastic properties [74]. Replicating this microstructure generation approach, we compute the effective elastic properties using the periodic staggered grid [32] as well as the staggered grid with zero Dirichlet boundary conditions using the approach presented in Section 3. The results obtained by Soyarslan et al. [93] as well as with the *rotated* staggered grid (Q1R) [73] serve as benchmarks. Figure 7 shows the shear modulus for various volume element

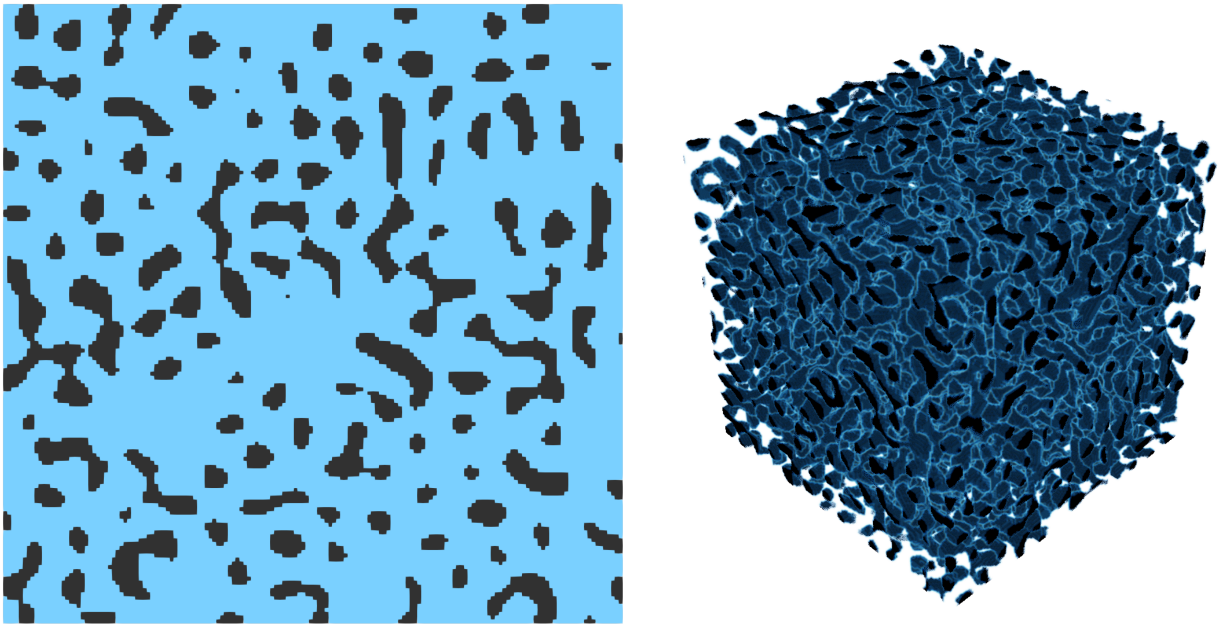

FIGURE 6 | A single phase of a 160^3 bicontinuous stochastic microstructure with a gold volume fraction of 20%. (a) Slice (gold shown in black), (b) 3D view.

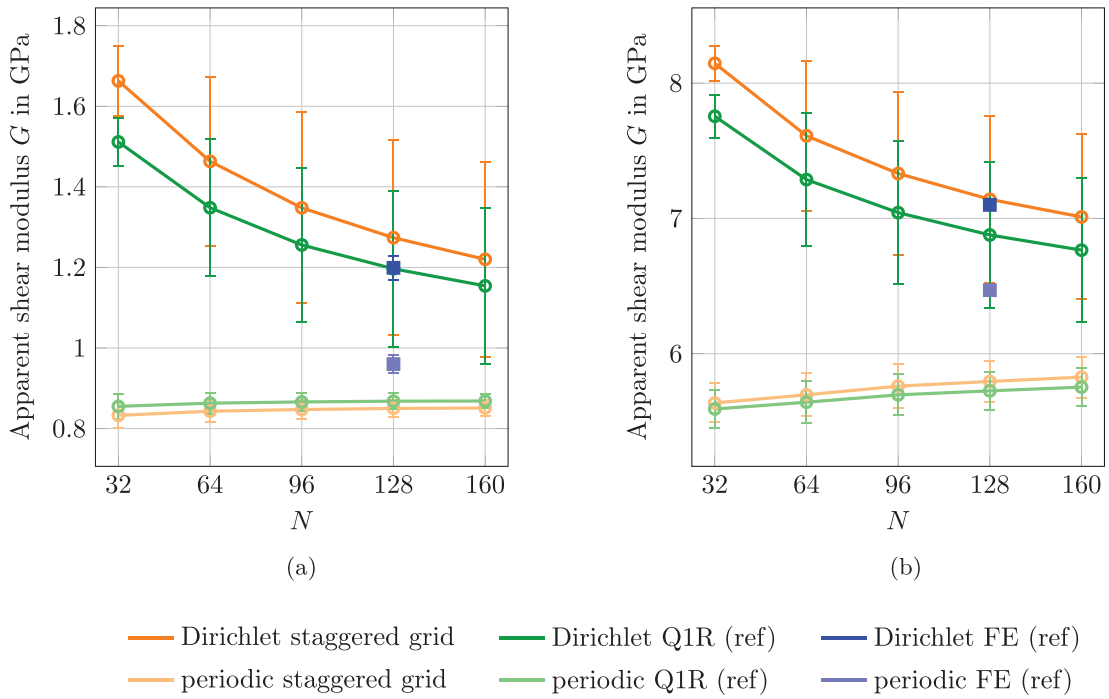

FIGURE 7 | Bicontinuous microstructure with different boundary conditions and various volume element sizes N^3, including reference values from Soyarslan et al. [93] for the FE results and Risthaus-Schneider [74] for the Q1R results. (a) Shear modulus for the bicontinuous microstructure with a gold volume fraction of 20%, (b) Shear modulus for the bicontinuous microstructure with a gold volume fraction of 50%.

sizes of the microstructure, computed from an isotropic approximation obtained from six load cases per microstructure. Comparing the results with Dirichlet boundary conditions, we observe a lower apparent shear modulus for the staggered grid discretization for both a gold volume fraction of 20% in Figure 7a as well as a gold volume fraction of 50% in Figure 7b. Independent of the discretization scheme selected, boundary effects lead to a noticeably increased standard deviation of the apparent moduli for Dirichlet boundary conditions compared to the periodic case [94]. For a gold volume fraction of 50% (Figure 7b), the mean apparent shear modulus computed with the staggered grid discretization is rather close to the value given by Soyarslan et al. [93] for a volume element size of 128^3. Interestingly, the value obtained by Soyarslan et al. [93] for a gold volume fraction of 50% is considerably closer matched by the results obtained using the Q1R discretization, with the staggered grid yielding a lower apparent shear modulus. This discrepancy is caused by the high standard deviation of the results and is rooted in the systematic error caused by the boundary effects. The results obtained by Soyarslan et al. [93] for periodic boundary conditions are consistently higher than the results obtained with either the staggered grid or Q1R discretization.

To sum up the results for this microstructure type, after investigating microstructures with finite material contrast for Dirichlet boundary conditions, we found a similar behavior of the staggered grid and the Q1R discretization. The results correlate well with results from the literature and show that the staggered grid predicts slightly lower apparent properties compared to FE-based discretization, like the Q1R discretization.

4.4 | Binder-Jetted Sand Core – Infinite Contrast

Sand cores are a crucial step in industrial casting processes, serving as the mold for cast parts [95, 96]. On a microstructure level, the binder-jetted sand cores consist of densely packed sand grains that are connected by small amounts of polymeric binders. We investigated the digital generation of binder-jetted sand core microstructures [50], an approach that shows promising results regarding the reproducibility of real-world experiments on sand core microstructures with periodic boundary conditions using FFT-based solvers. A sample microstructure is shown in Figure 8, where the sand grains are

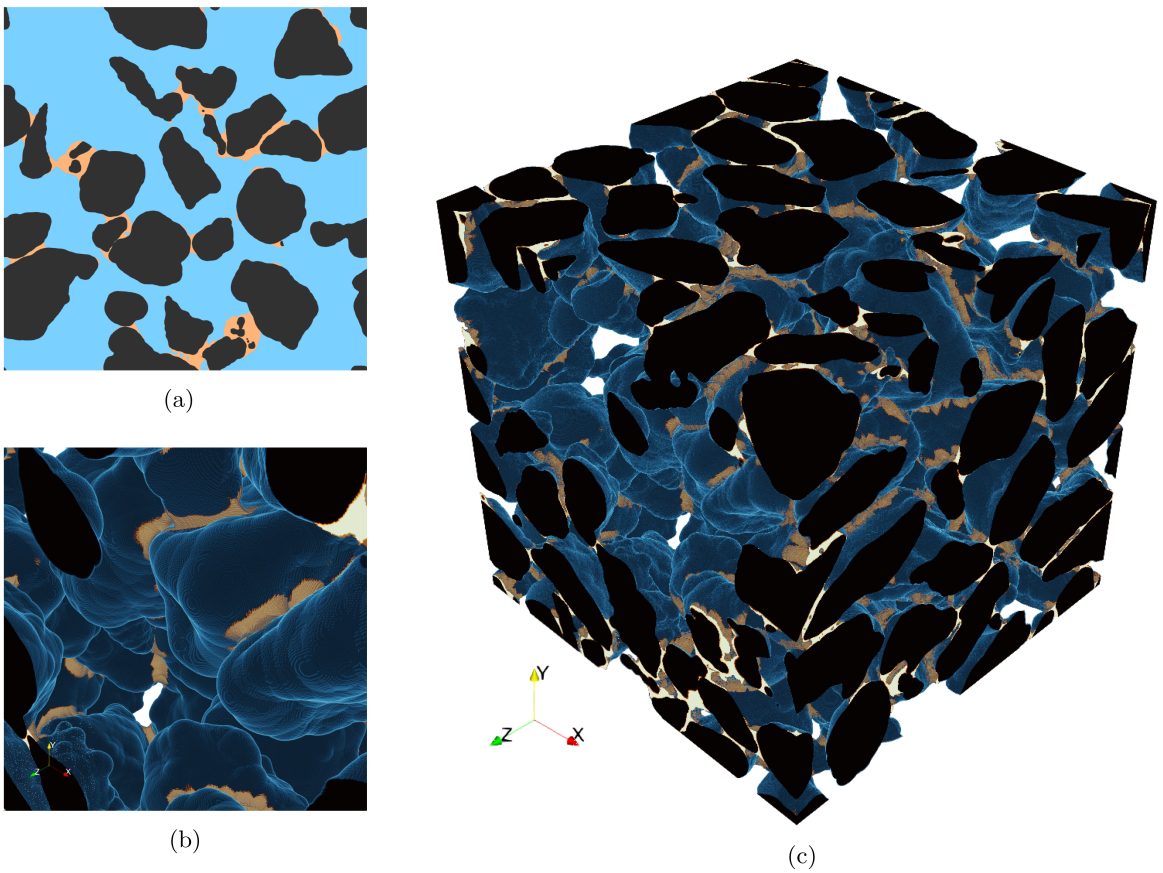

FIGURE 8 | 3D-printed sand core microstructure. The dark sand grains with a volume fraction of 50% are linked by binder in yellow with a volume fraction of 2%. (a) Slice in the xy-plane, void colored in blue, (b) detail of 3D view, and (c) 3D view.

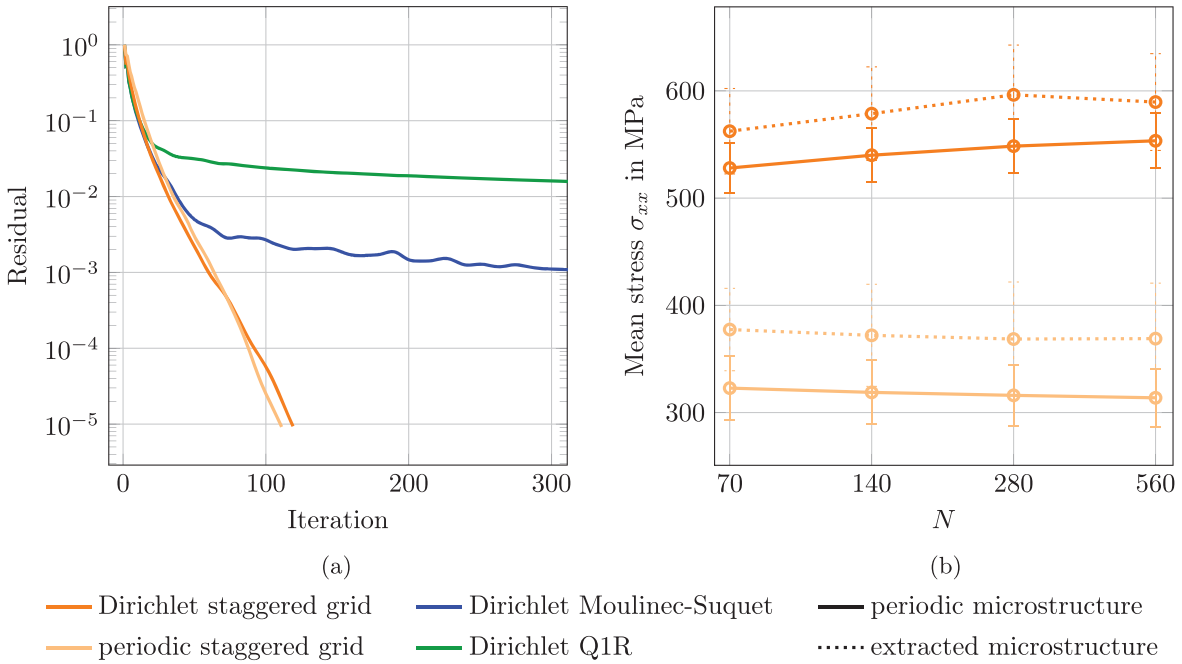

FIGURE 9 | Convergence plot and mean stress with Dirichlet boundary conditions for the sand core microstructure of cubic size 560μm for various resolutions N^3. (a) Residual versus iterations, (b) mean stress.

connected by a small amount of the yellow binder. Unlike conventional FE methods, FFT-based homogenization methods inherently operate on a regular grid. Therefore, due to the void phase between the sand grains, material points with zero stiffness cannot be circumvented, a fact that leads to slow or even no convergence for most discretization schemes with periodic boundary conditions [52]. In the periodic case, the staggered grid discretization allows us to compute the effective elastic properties of porous materials while most other discretizations fail to converge in a reasonable number of iterations [32]. Based on this fact, to investigate the binder-jetted sand core microstructure in a periodic setting, the authors chose the (periodic) staggered grid discretization for the FFT-based homogenization, which led to good convergence [50].

Inspired by this observation—using the staggered grid discretization with Dirichlet boundary conditions as introduced in this work—we want to investigate if the reduced convergence for other discretizations still holds in case Dirichlet boundary conditions are applied. We generate sand core microstructures using the Stacked MCM approach presented by Donval et al. [50, 97].

The convergence behavior of the linear CG solver with the staggered grid discretization and Dirichlet boundary conditions for microstructures with pores is shown in Figure 9a. We observe that for Dirichlet boundary conditions, the Q1R discretization as well as the Moulinec-Suquet discretization do not lead to convergence in a reasonable number of iterations. Conversely, the staggered grid discretization demonstrates a comparable convergence pattern for both Dirichlet and periodic boundary conditions. As was shown by the authors [72], employing the large-strain formulation (12) increases the condition number bound by a factor of two compared to the periodic small-strain case. This elevation, in turn, leads to an expected increase in the iteration count of the linear CG solver by a factor $\sqrt{2}$ compared to the periodic setting. Noticeably, we do not observe this rather stark increase in the iteration count, but only an increase from the 112 iterations of the periodic boundary conditions to 120 iterations for the Dirichlet boundary conditions to reach a residual below the tolerance 10^{-5}. In this particular instance, the infinite material contrast reduces the impact of the less favorable conditioning of the Dirichlet problem.

For the given microstructure, we perform a resolution study where the same sand grain microstructure of an edge length of 560μm is resolved with various resolution steps. We compare two types of microstructures. The first microstructure under consideration is a periodic microstructure that was generated to be periodic over all volume boundaries. The periodic microstructure is proven to perform favorably in regard to its apparent properties when combined with periodic boundary conditions and leads to rather small representative volume elements [94]. The second microstructure is a so-called "extracted" microstructure, which was obtained by a cut-out from a larger microstructure image. This microstructure is not periodic and serves as a proxy for microstructures obtained by real-life scans. Figure 9b shows the apparent mean stress

σ_{xx} for an applied mean strain $\epsilon_{xx} = 5\%$ computed as the mean of ten realizations. Like for the previous example with finite contrast in Section 4.3, we observe a noticeably higher apparent stiffness for the Dirichlet boundary conditions independent of the resolution [55]. For both periodic and Dirichlet boundary conditions, the extracted microstructures yield higher apparent stiffnesses. In relative terms, the increase of stiffness by the extracted microstructure is higher for periodic boundary conditions, as the combination of periodic boundary conditions and periodic microstructure is not subject to boundary effects [94]. For Dirichlet boundary conditions, the resolution has a stronger influence on the apparent stiffness. Even the highest resolution $N = 560$ shows a slightly higher stiffness compared to the value for the second-highest resolution step $N = 280$. Due to the impact of boundary effects, the apparent properties computed with Dirichlet boundary conditions have a higher sensitivity to the resolution. This characteristic, in turn, makes it less favorable for general tasks to approximate effective properties.

4.5 | Polymer Foam – Infinite Contrast

A polymer foam microstructure serves as a final benchmark of the framework. Polymer foams have numerous applications in engineering [46, 47] due to their low thermal conductivity and favorable specific stiffness. This microstructure type is another challenging example with infinite material contrast.

The microstructure is generated from a Laguerre tessellation of the microstructure whose sites are based on a sphere packing [98–100]. Instead of simply shrinking the cell of the Laguerre tessellation [101, 102], in a second step, the surface area of the individual cells is reduced by a level set morphing, leading to a foam microstructure with rounded, yet non-spherical cells. An example microstructure is shown in Figure 10. The foam cell generation approach under consideration results in the formation of thin walls on the surfaces that connect two cells. Therefore, resolving these features is not always possible for any given resolution, leading to the holes in the centers of the cell faces. To study the effect of the resolution on the effective elastic properties, we perform a resolution study on a single polymer foam microstructure. The enhanced resolution of thin features is evident in Figure 11, where the same slice of the foam is shown at multiple resolution levels.

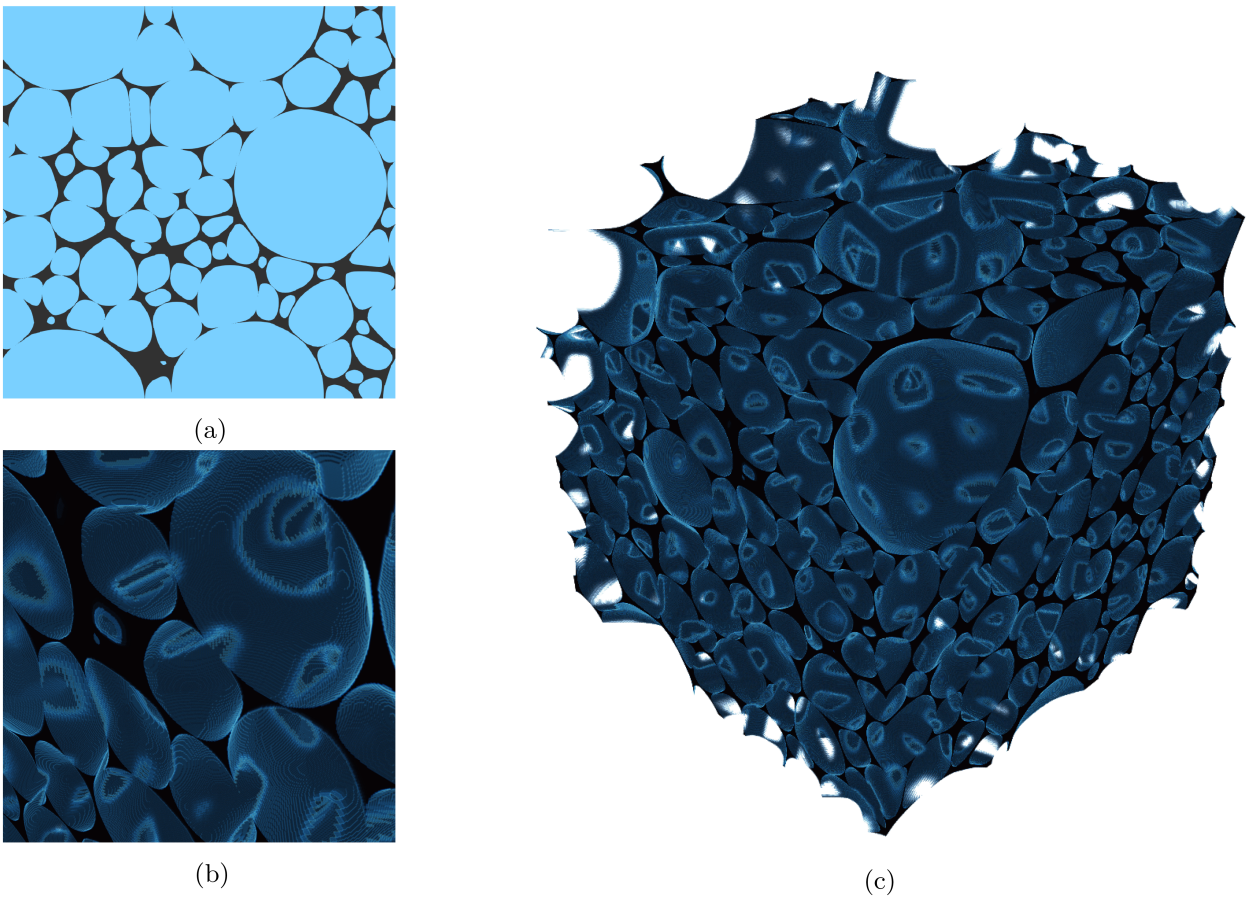

FIGURE 10 | Foam microstructure. (a) Slice, (b) detail of 3D view, and (c) 3D view.

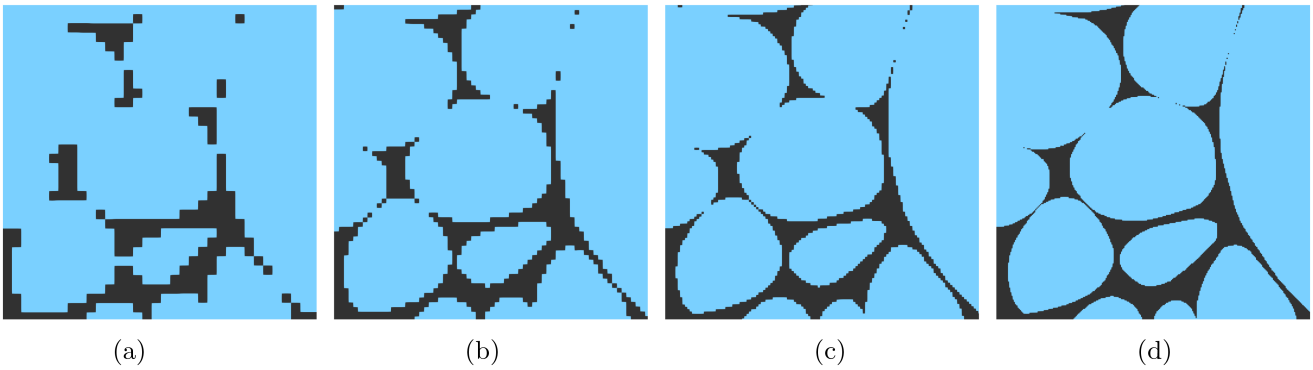

FIGURE 11 | Detail of a 2D slice of a polymer foam microstructure for various resolutions. (a) 128^3, (b) 256^3, (c) 512^3, and (d) 1024^3.

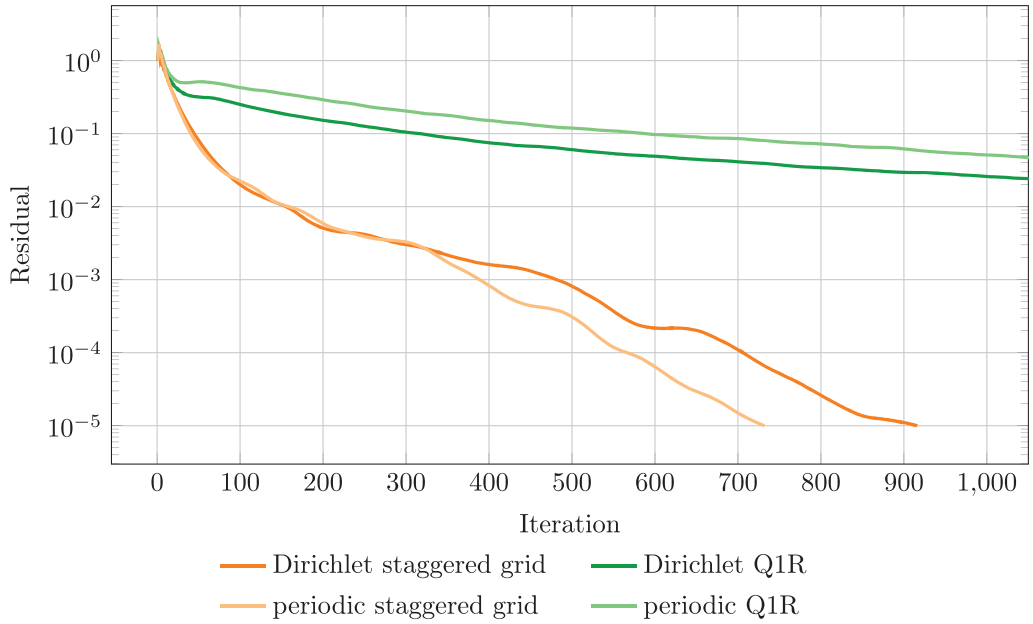

FIGURE 12 | Residual versus iteration for $N = 128$ and linear CG.

To rule out any influence of the volume fraction, we fix the polymer volume fraction at 5% when generating the voxelized microstructure. The polymer's linear elastic material parameters are a Young's modulus of $E = 3.0$ and Poisson's ratio of $\nu = 0.25$. Figure 12 shows the convergence of the CG solver. We observe that the staggered grid converges robustly for both periodic and Dirichlet boundary conditions, whereas the Q1R discretization diverges. The staggered grid with Dirichlet boundary conditions needs noticeably more iterations with 917 versus the 733 iterations for the periodic staggered grid, an increase in line with the increase in CG iterations we expect from theory by a factor $\sqrt{2}$.

Figure 13a shows the mean stress for the staggered grid and both types of boundary conditions. Like in the previous examples, Dirichlet boundary conditions lead to a higher apparent stress. Both types of boundary conditions cause a stark increase in apparent stiffness for increased resolution. Even though the volume fraction of polymer is not increased, the stronger connectivity leads to a higher apparent stiffness.

As for the sand core microstructure in Section 4.4, we performed the same experiment with extracted microstructures as well, which serve as a proxy for real microstructure image, obtained from scans of real materials.

Dirichlet boundary conditions result in a significantly higher apparent stiffness compared to the periodic case. Conversely, for periodic boundary conditions, the apparent stiffness of the extracted microstructure is actually lower. The reduced connectivity of low resolutions decreases the apparent stiffness of a foam. Similarly, the reduced connectivity of the microstructure on the volume element boundaries also decreases the apparent properties [72, 94].

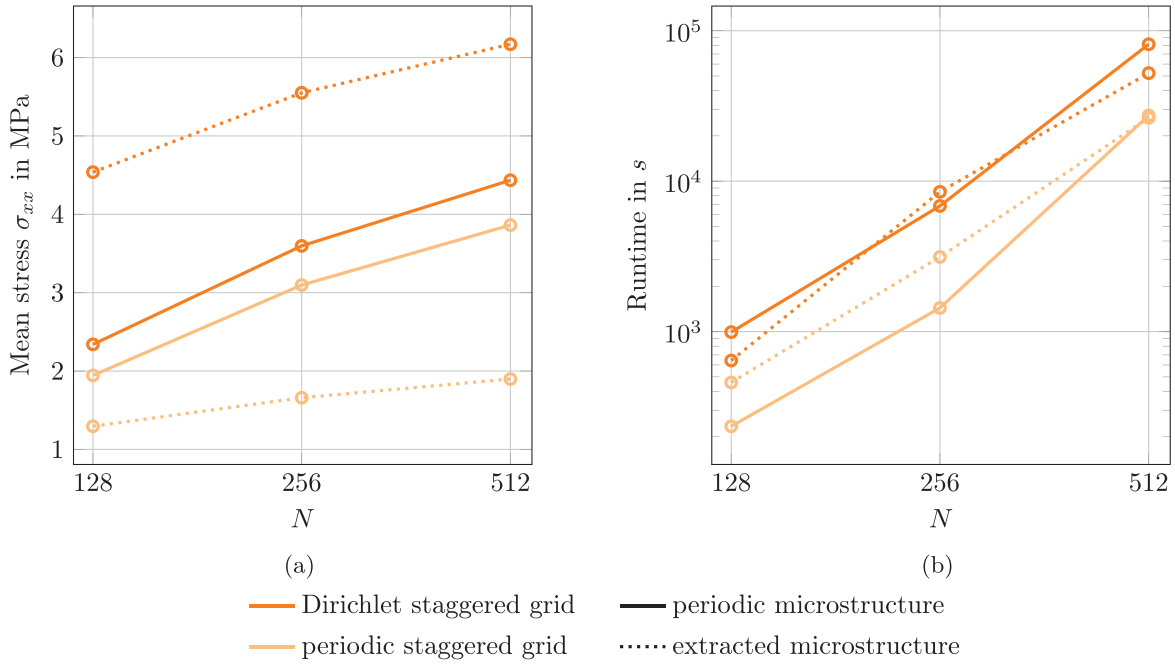

FIGURE 13 | Apparent mean stress and runtimes for the polymer foam microstructure. (a) Mean stress σ_{xx}, (b) runtimes.

The runtimes to compute the apparent properties computed on four threads are shown in Figure 13b. In this case, the runtimes for the Dirichlet case remain competitive compared to other homogenization approaches and scale well with resolution increase. However, they are considerably higher than the runtimes with periodic boundary conditions.

5 | Conclusion

In the article at hand, we introduced a computational strategy for imposing Dirichlet boundary conditions for FFT-based homogenization using the staggered grid discretization. The staggered grid discretization features multiple advantageous properties. Only one evaluation of the material law per voxel is necessary, reducing the computational cost imposed by the material law evaluation. Additionally, the staggered grid enables FFT-based solvers to converge robustly for microstructures with infinite material contrast.

Combining the authors' bottom-up approach [62, 72, 73] of imposing Dirichlet boundary conditions in classical FFT-based homogenization frameworks was a natural step, which came with some challenges. The non-centered locations of the degrees of freedom on the staggered grid made the introduction of a shift operation necessary. Furthermore, uneven lengths of the axes required a cautionary adaptation of the discrete sine and cosine transforms and of the range of summation for the computation of averages. To this end, we highlighted the necessary alterations to an existing FFT-based solver and showed in detail how to implement these changes in a fast and robust manner. Due to the applicability of this approach to microstructures with voids or pores, this work forms a basis for reliable industrial applications. As examples for the versatility of the approach, we showed various numerical experiments, starting from finite contrast examples, where we demonstrated the ringing-free local fields as well as the good convergence behavior when combining Dirichlet boundary conditions and the staggered grid. A comparison with values from the literature provided validation of the computed properties. Therefore, the presented approach constitutes a genuine alternative to FE-based homogenization approaches, particularly for the homogenization step of FE^2 solvers. Finally, the ability of the staggered grid with Dirichlet boundary conditions to handle infinite contrast microstructures was shown with two examples with an increasing volume fraction of voids. Both the sand core and the foam microstructure example showed a good convergence speed with Dirichlet boundary conditions, with a slight, but expected reduction in convergence speed in cases where periodic boundary conditions are not applicable, that is, non-periodic microstructures with low volume fractions of solid material [73].

The last example of the polymer foam in Section 4.5 highlights a use-case of Dirichlet boundary conditions in combination with FFT-based homogenization. The apparent properties of an extracted (non-periodic) microstructure are considerably underestimated by periodic boundary conditions. Even though the Dirichlet boundary conditions in turn overestimate the

apparent properties, Dirichlet boundary conditions serve to obtain an upper bound for the stiffness of the foam. Employing other solution methods, such as conventional FE, would be considerably more resource-intensive than the FFT-based approach at hand, especially when aiming to resolve the thin features of a polymeric foam.

Applying Dirichlet boundary conditions comes with increased runtimes. This slowdown is rooted in both the slower performance of the DCT and DST compared to the periodic FFT, as well as in the need to compute the large-strain Eshelby-Green operator. In the periodic case, the mean can be conveniently computed and set as the zero-frequency value in Fourier space, whereas the same approach is not applicable with Dirichlet boundary conditions, leading to a performance overhead. Further research might overcome this flaw and should enable combined periodic and Dirichlet boundary conditions with the staggered grid on different faces of the volume element. This flexibility enables a true validation using experimental results [57, 71]. An extension of FFT-based homogenization with non-periodic boundary conditions in combination with composite voxels [79, 81] or extended finite elements (XFEM) [103] promises better approximation behavior for low resolutions.

In a completely different direction, recent work ([104], § 9) tries to learn non-local constitutive laws [105, 106] via machine learning techniques driven by body forces with compact support, providing a flexible and scalable alternative to obtaining local effective material behavior. It might be of interest to extend FFT solvers to cover such cases.

Acknowledgments

The authors thank M. Kabel (ITWM) for insisting on the importance of the topic and providing helpful feedback. M.S. acknowledges support from the European Research Council within the Horizon Europe program—project no. 101040238. We thank the anonymous reviewers for their effort and their constructive remarks. Open Access funding enabled and organized by Projekt DEAL.

Data Availability Statement

The data that support the findings of this study are available from the corresponding author upon reasonable request.

References

1. H. Moulinec and P. Suquet, "A Fast Numerical Method for Computing the Linear and Nonlinear Mechanical Properties of Composites," *Comptes Rendus de L'académie Des Sciences. Série II* 318, no. 11 (1994): 1417–1423.

2. H. Moulinec and P. Suquet, "A Numerical Method for Computing the Overall Response of Nonlinear Composites With Complex Microstructure," *Computer Methods in Applied Mechanics and Engineering* 157 (1998): 69–94.

3. M. Kabel, T. Böhlke, and M. Schneider, "Efficient Fixed Point and Newton-Krylov Solvers for FFT-Based Homogenization of Elasticity at Large Deformations," *Computational Mechanics* 54, no. 6 (2014): 1497–1514.

4. J. Barzilai and J. M. Borwein, "Two-point step size gradient methods," *IMA Journal of Numerical Analysis* 8 (1988): 141–148.

5. M. Schneider, "On the Barzilai-Borwein Basic Scheme in FFT-Based Computational Homogenization," *International Journal for Numerical Methods in Engineering* 118, no. 8 (2019): 482–494.

6. Y. Nesterov, "A Method for Solving the Convex Programming Problem With Convergence Rate $O\left(1/k^2\right)$," *Dokladi Akademii Nauk SSSR* 269, no. 3 (1983): 543–547.

7. M. Schneider, "An FFT-Based Fast Gradient Method for Elastic and Inelastic Unit Cell Homogenization Problems," *Computer Methods in Applied Mechanics and Engineering* 315 (2017): 846–866.

8. M. Hestenes and E. Stiefel, "Methods of Conjugate Gradients for Solving Linear Systems," *Journal of Research of the National Bureau of Standards* 49 (1952): 409–436.

9. S. Brisard and L. Dormieux, "FFT-Based Methods for the Mechanics of Composites: A General Variational Framework," *Computational Materials Science* 49, no. 3 (2010): 663–671.

10. J. Zeman, J. Vondřejc, J. Novák, and I. Marek, "Accelerating a FFT-Based Solver for Numerical Homogenization of Periodic Media by Conjugate Gradients," *Journal of Computational Physics* 229, no. 21 (2010): 8065–8071.

11. M. Schneider, "A Dynamical View of Nonlinear Conjugate Gradient Methods With Applications to FFT-Based Computational Micromechanics," *Computational Mechanics* 66 (2020): 239–257.

12. N. Lahellec, J. C. Michel, H. Moulinec, and P. Suquet, "Analysis of Inhomogeneous Materials at Large Strains Using Fast Fourier Transforms," in *IUTAM Symposium on Computational Mechanics of Solid Materials at Large Strains. Solid Mechanics and Its Applications*, vol. 108, ed. C. Miehe (Springer Netherlands, 2003), 247–258.

13. D. Wicht, M. Schneider, and T. Böhlke, "On Quasi-Newton Methods in FFT-Based Micromechanics," *International Journal for Numerical Methods in Engineering* 121, no. 8 (2020): 1665–1694.

14. Y. Chen, L. Gélébart, C. Chateau, M. Bornert, C. Sauder, and A. King, "Analysis of the Damage Initiation in a SiC/SiC Composite Tube From a Direct Comparison Between Large-Scale Numerical Simulation and Synchrotron X-Ray Micro-Computed Tomography," *International Journal of Solids and Structures* 161 (2019): 111–126.

15. V. Monchiet and G. Bonnet, "A Polarization-Based FFT Iterative Scheme for Computing the Effective Properties of Elastic Composites With Arbitrary Contrast," *International Journal for Numerical Methods in Engineering* 89 (2012): 1419–1436.

16. V. Monchiet and G. Bonnet, "Numerical Homogenization of Nonlinear Composites With a Polarization-Based FFT Iterative Scheme," *Computational Materials Science* 79 (2013): 276–283.

17. H. Moulinec and F. Silva, "Comparison of Three Accelerated FFT-Based Schemes for Computing the Mechanical Response of Composite Materials," *International Journal for Numerical Methods in Engineering* 97 (2014): 960–985.

18. D. Wicht, M. Schneider, and T. Böhlke, "An Efficient Solution Scheme for Small-Strain Crystal-Elasto-Viscoplasticity in a Dual Framework," *Computer Methods in Applied Mechanics and Engineering* 358 (2020): 112611.

19. K. P. Herrmann, W. H. Müller, and S. Neumann, "Linear and Elastic-Plastic Fracture Mechanics Revisited by Use of Fourier Transforms: Theory and Application," *Computational Materials Science* 6 (1999): 186–196.

20. J. Li, S. Meng, X. Tian, F. Song, and C. Jiang, "An Non-Local Fracture Model for Composite Laminates and Numerical Simulations by Using the FFT Method," *Composites Part B: Engineering* 43 (2012): 961–971.

21. J. Li, X.-X. Tian, and R. Abdelmoula, "A Damage Model for Crack Prediction in Brittle and Quasi-Brittle Materials Solved by the FFT Method," *International Journal of Fracture* 173 (2012): 135–146.

22. V. Monchiet, G. Bonnet, and G. Lauriat, "A FFT-Based Method to Compute the Permeability Induced by a Stokes Slip Flow Through a Porous Medium," *Comptes Rendus Mécanique* 337, no. 4 (2009): 192–197.

23. F. Bignonnet and L. Dormieux, "FFT-Based Bounds on the Permeability of Complex Microstructures," *International Journal for Numerical and Analytical Methods in Geomechanics* 38 (2014): 1707–1723.

24. B. Abdallah, F. Willot, and D. Jeulin, "Stokes Flow Through a Boolean Model of Spheres: Representative Volume Element," *Transport in Porous Media* 109 (2015): 711–726.

25. J. Segurado and R. A. Lebensohn, "An FFT-Based Approach for Bloch Wave Analysis: Application to Polycrystals," *Computational Mechanics* 68 (2021): 981–1001.

26. R. Sancho, V. R. de Pedraza, P. Lafourcade, R. A. Lebensohn, and J. Segurado, "An Implicit FFT-Based Method for Wave Propagation in Elastic Heterogeneous Media," *Computer Methods in Applied Mechanics and Engineering* 404 (2023): 115772.

27. J. Vondřejc, J. Zeman, and I. Marek, "An FFT-Based Galerkin Method for Homogenization of Periodic Media," *Computers & Mathematics with Applications* 68, no. 3 (2014): 156–173.

28. M. Schneider, "On the Effectiveness of the Moulinec-Suquet Discretization for Composite Materials," *International Journal for Numerical Methods in Engineering* 124, no. 14 (2023): 3191–3218.

29. S. Abarbanel, D. Gottlieb, and E. Tadmor, "Spectral Methods for Discontinuous Problems," in *Numerical Methods for Fluid Dynamics II*, ed. K. Morton and M. Baines (Oxford University Press, 1986), 128–153.

30. W. H. Müller, "Mathematical vs. Experimental Stress Analysis of Inhomogeneities in Solids," *Journal De Physique. IV, Colloque* 6 (1996): C1.139–C1.148.

31. W. H. Müller, "Fourier Transforms and Their Application to the Formation of Textures and Changes of Morphology in Solids," in *IUTAM Symposium on Transformation Problems in Composite and Active Materials*, vol. 60, ed. Y. A. Bahei-El-Din and G. J. Dvorak (Kluwer, 1998), 61–72.

32. M. Schneider, F. Ospald, and M. Kabel, "Computational Homogenization of Elasticity on a Staggered Grid," *International Journal for Numerical Methods in Engineering* 105, no. 9 (2016): 693–720.

33. F. Willot, "Fourier-Based Schemes for Computing the Mechanical Response of Composites With Accurate Local Fields," *Comptes Rendus Mécanique* 343 (2015): 232–245.

34. S. Brisard and L. Dormieux, "Combining Galerkin Approximation Techniques With the Principle of Hashin and Shtrikman to Derive a New FFT-Based Numerical Method for the Homogenization of Composites," *Computer Methods in Applied Mechanics and Engineering* 217–220 (2012): 197–212.

35. M. Schneider, D. Merkert, and M. Kabel, "FFT-Based Homogenization for Microstructures Discretized by Linear Hexahedral Elements," *International Journal for Numerical Methods in Engineering* 109 (2017): 1461–1489.

36. J. Zeman, T. W. J. de Geus, J. Vondřejc, R. H. J. Peerlings, and M. G. D. Geers, "A Finite Element Perspective on Nonlinear FFT-Based Micromechanical Simulations," *International Journal for Numerical Methods in Engineering* 111 (2017): 903–926.

37. J. Yvonnet, "A Fast Method for Solving Microstructural Problems Defined by Digital Images: A Space Lippmann–Schwinger Scheme," *International Journal for Numerical Methods in Engineering* 92, no. 2 (2012): 178–205.

38. M. Leuschner and F. Fritzen, "Fourier-Accelerated Nodal Solvers (FANS) for Homogenization Problems," *Computational Mechanics* 62 (2018): 359–392.

39. M. Ladecký, R. J. Leute, A. Falsafi, et al., "An Optimal Preconditioned FFT-Accelerated Finite Element Solver for Homogenization," *Applied Mathematics and Computation* 446 (2023): 127835.

40. D. P. Flanagan and T. Belytschko, "A Uniform Strain Hexahedron and Quadrilateral With Orthogonal Hourglass Control," *International Journal for Numerical Methods in Engineering* 17 (1981): 679–706.

41. M. Schneider, "Voxel-Based Finite Elements With Hourglass Control in FFT-Based Computational Homogenization," *International Journal for Numerical Methods in Engineering* 123, no. 24 (2022): 6286–6313.

42. C. Dorn and M. Schneider, "Lippmann-Schwinger Solvers for the Explicit Jump Discretization for Thermal Computational Homogenization Problems," *International Journal for Numerical Methods in Engineering* 118, no. 11 (2019): 631–653.

43. F. Ernesti and M. Schneider, "A Fast Fourier Transform Based Method for Computing the Effective Crack Energy of a Heterogeneous Material on a Combinatorially Consistent Grid," *International Journal for Numerical Methods in Engineering* 122, no. 21 (2021): 6283–6307.

44. M. R. Derraz, M. Boukour, A. El Mamouni, and A. El Omri, "Three-Dimensional Finite Radon Transform and Linear Homogenization," in *Advanced Intelligent Systems for Sustainable Development (AI2SD'2020)*. Advances in Intelligent Systems and Computing, vol. 1418, ed. J. Kycprzyk, V. E. Balas, and M. Ezziyyani (Springer International Publishing, 2022), 164–182.

45. L. Jabs and M. Schneider, "A Consistent Discretization via the Finite Radon Transform for FFT-Based Computational Micromechanics," *Computational Mechanics* 75 (2024): 1451–1470.

46. M. Dabo, T. Roland, G. Dalongeville, C. Gauthier, and P. Kékicheff, "Ad-Hoc Modeling of Closed-Cell Foam Microstructures for Structure-Properties Relationships," *European Journal of Mechanics - A/Solids* 75 (2019): 128–141.

47. F. M. de Souza, Y. Desai, and R. K. Gupta, *Introduction to Polymeric Foams*. ACS Symposium Series, vol. 1439 (American Chemical Society, 2023), 1–23.

48. W. Pabst, T. Uhlířová, E. Gregorová, and A. Wiegmann, "Relative Young's Modulus and Thermal Conductivity of Isotropic Porous Ceramics With Randomly Oriented Spheroidal Pores – Model-Based Relations, Cross-Property Predictions and Numerical Calculations," *Journal of the European Ceramic Society* 38, no. 11 (2018): 4026–4034.

49. P. Šimonová, T. Uhlířová, and W. Pabst, "Computer Modeling of Young's Modulus and Thermal Conductivity Changes During Sintering Without Shrinkage," *Journal of the European Ceramic Society* 43, no. 11 (2023): 4885–4895.

50. E. Donval, M. Schneider, H. Grimm-Strele, et al., "A Directional Contraction Method to Model Sand-Based Binder Jet 3D Printed Materials," *International Journal of Solids and Structures* 312 (2025): in press 113260.

51. M. Schneider, "Lippmann-Schwinger Solvers for the Computational Homogenization of Materials With Pores," *International Journal for Numerical Methods in Engineering* 121, no. 22 (2020): 5017–5041.

52. M. Schneider, "A Review of Non-Linear FFT-Based Computational Homogenization Methods," *Acta Mechanica* 232 (2021): 2051–2100.

53. R. A. Lebensohn and A. D. Rollett, "Spectral Methods for Full-Field Micromechanical Modelling of Polycrystalline Material," *Computational Materials Science* 173 (2020): 109336.

54. C. Gierden, J. Kochmann, J. Waimann, B. Svendsen, and S. Reese, "A Review of FE-FFT-Based Two-Scale Methods for Computational Modeling of Microstructure Evolution and Macroscopic Material Behavior," *Archives of Computational Methods in Engineering* 29 (2022): 4115–4135.

55. R. Hill, "Elastic Properties of Reinforced Solids: Some Theoretical Principles," *Journal of the Mechanics and Physics of Solids* 11, no. 5 (1963): 357–372.

56. F. Bödeker, P. Herr, R. Moshfegh, A. Biel, and S. Marzi, "A Novel FFT-Based Homogenization Scheme for Cohesive Zones," *Procedia Structural Integrity* 42 (2022): 490–497.

57. F. Bödeker, P. Herr, A. Biel, R. Moshfegh, and S. Marzi, "An FFT-Based Homogenization Scheme for Cohesive Zones With an Application to Adhesives and the Core Material of Thin Metal Sandwich Plates," *Theoretical and Applied Fracture Mechanics* 129 (2022): 104186.

58. L. Gélébart, "A Modified FFT-Based Solver for the Mechanical Simulation of Heterogeneous Materials With Dirichlet Boundary Conditions," *Comptes Rendus Mécanique* 348, no. 8–9 (2020): 693–704.

59. N. B. Nkoumbou Kaptchouang and L. Gélébart, "Multiscale Coupling of FFT-Based Simulations With the LDC Approach," *Computer Methods in Applied Mechanics and Engineering* 394 (2022): 114921.

60. A. Wathen, "Preconditioning," *Acta Numerica* 24 (2015): 329–376.

61. W. H. Press, S. A. Teukolsky, W. T. Vetterling, and B. P. Flannery, *Numerical Recipes in C - The Art of Scientific Computing* (Cambridge University Press, 2007).

62. L. Risthaus and M. Schneider, "Imposing Different Boundary Conditions for Thermal Computational Homogenization Problems With FFT- and Tensor-Train-Based Green's Operator Methods," *International Journal for Numerical Methods in Engineering* 125, no. 7 (2024): e7423.

63. V. Monchiet and G. Bonnet, "FFT Based Iterative Schemes for Composite Conductors With Uniform Boundary Conditions," *European Journal of Mechanics - A/Solids* 103 (2024): 105146.

64. L. Morin and J. Paux, "A Fast Numerical Method for the Conductivity of Heterogeneous Media With Dirichlet Boundary Conditions Based on Discrete Sine–Cosine Transforms," *Computer Methods in Applied Mechanics and Engineering* 421 (2024): 116772.

65. L. Gelebart, "FFT-Based Simulations of Heterogeneous Conducting Materials With Combined Non-Uniform Neumann, Periodic and Dirichlet Boundary Conditions," *European Journal of Mechanics - A/Solids* 105 (2024): 105248.

66. J. Paux, L. Morin, and L. Gélébart, "A Discrete Sine-Cosine Transforms Galerkin Method for the Conductivity of Heterogeneous Materials With Mixed Dirichlet/Neumann Boundary Conditions," *International Journal for Numerical Methods in Engineering* 126, no. 1 (2025): e7615.

67. A. Finel, "A tetrahedron-based discretization for FFT-based computational homogenization with smooth solution fields," *Computer Methods in Applied Mechanics and Engineering* 436 (2025): 117703.

68. L. Gélébart, "An Accurate and Robust FFT-Based Solver for Transient Diffusion in Heterogeneous Materials," *Comptes Rendus. Mécanique* 353 (2025): 113–125.

69. A. Wiegmann, *Fast Poisson, Fast Helmholtz and Fast Linear Elastostatic Solvers on Rectangular Parallelepipeds Technical Report*, vol. LBNL-43565 (Lawrence Berkeley National Laboratory, 1999), 1–21.

70. D. H. Pahr and P. K. Zysset, "Influence of Boundary Conditions on Computed Apparent Elastic Properties of Cancellous Bone," *Biomechanics and Modeling in Mechanobiology* 7, no. 6 (2021): 463–476.

71. H. Grimm-Strele and M. Kabel, "FFT-Based Homogenization With Mixed Uniform Boundary Conditions," *International Journal for Numerical Methods in Engineering* 122 (2021): 7241–7265.

72. L. Risthaus and M. Schneider, "Imposing Dirichlet Boundary Conditions Directly for FFT-Based Computational Micromechanics," *Computational Mechanics* 74, no. 5 (2024): 1089–1113.

73. L. Risthaus and M. Schneider, "FFT-Based Computational Micromechanics With Dirichlet Boundary Conditions on the Rotated Staggered Grid," *International Journal for Numerical Methods in Engineering* 125, no. 21 (2024): e7569.

74. L. Risthaus and M. Schneider, "Dirichlet Boundary Conditions for FFT-Based Micromechanics of Bicontinuous Stochastic Microstructures," *PAMM* 24, no. 4 (2024): e202400182.

75. J. Paux, L. Morin, L. Gélébart, and A. M. Amadou Sanoko, "A Discrete Sine-Cosine Based Method for the Elasticity of Heterogeneous Materials With Arbitrary Boundary Conditions," *Computer Methods in Applied Mechanics and Engineering* 433 (2025): 117488.

76. F. H. Harlow and J. E. Welch, "Numerical Calculation of Time-Dependent Viscous Incompressible Flow of Fluid With Free Surface," *Physics of Fluids* 8 (1965): 2182–2189.

77. Y. Zhu, S. E. J. Teran, and A. Brandt, "An Efficient Parallelizable Multigrid Framework for the Simulation of Elastic Solids," *ACM Transactions on Graphics* 29 (2010): 1–18.

78. M. Frigo and S. G. Johnson, "The Design and Implementation of FFTW3," *Proceedings of the IEEE* 93 (2005): 216–231.

79. M. Kabel, D. Merkert, and M. Schneider, "Use of Composite Voxels in FFT-Based Homogenization," *Computer Methods in Applied Mechanics and Engineering* 294 (2015): 168–188.

80. F. Ospald, M. Schneider, and M. Kabel, "A Model Order Reduction Method for Computational Homogenization at Finite Strains on Regular Grids Using Hyperelastic Laminates to Approximate Interfaces," *Computer Methods in Applied Mechanics and Engineering* 309 (2016): 476–496.

81. J. Lendvai and M. Schneider, "Assumed Strain Methods in Micromechanics, Laminate Composite Voxels and Level Sets," *International Journal for Numerical Methods in Engineering* 125, no. 11 (2024): e7459.

82. J. Hattel and P. Hansen, "A Control Volume-Based Finite Difference Method for Solving the Equilibrium Equations in Terms of Displacements," *Applied Mathematical Modelling* 19, no. 4 (1995): 210–243.

83. J. W. Cahn and J. E. Hilliard, "Free Energy of a Nonuniform System. I. Interfacial Free Energy," *Journal of Chemical Physics* 28, no. 2 (1958): 258–267.

84. A. Vidyasagar, S. Krödel, and D. M. Kochmann, "Microstructural Patterns With Tunable Mechanical Anisotropy Obtained by Simulating Anisotropic Spinodal Decomposition," *Proceedings of the Royal Society A: Mathematical, Physical and Engineering Sciences* 474, no. 2218 (2018): 20180535.

85. L. Risthaus and M. Schneider, "Solving Phase-Field Models in the Tensor Train Format to Generate Microstructures of Bicontinuous Composites," *Applied Numerical Mathematics* 178 (2022): 262–279.

86. J. W. Cahn, "On spinodal decomposition," *Acta Metallurgica* 9, no. 9 (1961): 795–801.

87. D. Blömker, S. Maier-Paape, and T. Wanner, "Spinodal Decomposition for the Cahn-Hilliard-Cook Equation," *Communications in Mathematical Physics* 223, no. 3 (2001): 553–582.

88. K. Wang and J. Weissmüller, "Composites of Nanoporous Gold and Polymer," *Advanced Materials* 25, no. 9 (2013): 1280–1284.

89. S. Bargmann, C. Soyarslan, E. Husser, and N. Konchakova, "Materials Based Design of Structures: Computational Modeling of the Mechanical Behavior of Gold-Polymer Nanocomposites," *Mechanics of Materials* 94 (2016): 53–65.

90. C. Richert and N. Huber, "A Review of Experimentally Informed Micromechanical Modeling of Nanoporous Metals: From Structural Descriptors to Predictive Structure–Property Relationships," *Materials* 13 (2020): 3307.

91. S. Kumar, S. Tan, L. Zheng, and D. M. Kochmann, "Inverse-designed spinodoid metamaterials," *npj Computational Materials* 6, no. 1 (2020): 1–10.

92. A. Raßloff, P. Seibert, K. A. Kalina, and M. Kästner, "Inverse Design of Spinodoid Structures Using Bayesian Optimization," arXiv 2402.13054 2024.

93. C. Soyarslan, M. Pradas, and S. Bargmann, "Effective Elastic Properties of 3D Stochastic Bicontinuous Composites," *Mechanics of Materials* 137 (2019): 103098.

94. M. Schneider, M. Josien, and F. Otto, "Representative Volume Elements for Matrix-Inclusion Composites - a Computational Study on the Effects of an Improper Treatment of Particles Intersecting the Boundary and the Benefits of Periodizing the Ensemble," *Journal of the Mechanics and Physics of Solids* 158 (2022): 104652.

95. M. Upadhyay, T. Sivarupan, and M. El Mansori, "3D Printing for Rapid Sand Casting–A Review," *Journal of Manufacturing Processes* 29 (2017): 211–220.

96. T. Sivarupan, N. Balasubramani, P. Saxena, et al., "A Review on the Progress and Challenges of Binder Jet 3D Printing of Sand Moulds for Advanced Casting," *Additive Manufacturing* 40 (2021): 101889.

97. S. Williams and A. Philipse, "Random Packings of Spheres and Spherocylinders Simulated by Mechanical Contraction," *Physical Review E* 67 (2003): 1–9.

98. K. A. Brakke, "The Surface Evolver," *Experimental Mathematics* 1, no. 2 (1992): 141–165.

99. C. Lautensack and S. Zuyev, "Random Laguerre Tessellations," *Advances in Applied Probability* 40, no. 3 (2008): 630–650.

100. A. Jung, C. Redenbach, K. Schladitz, and S. Staub, *3D Image-Based Stochastic Micro-Structure Modelling of Foams for Simulating Elasticity* (Springer International Publishing, 2022), 257–281.

101. C. Lautensack, "Fitting Three-Dimensional Laguerre Tessellations to Foam Structures," *Journal of Applied Statistics* 35, no. 9 (2008): 985–995.

102. H. S. Abdullahi, Y. Liang, and S. Gao, "Predicting the Elastic Properties of Closed-Cell Aluminum Foams: A Mesoscopic Geometric Modeling Approach," *SN Applied Sciences* 1 (2019): 380.

103. F. Gehrig and M. Schneider, "An X-FFT Solver for Two-Dimensional Thermal Homogenization Problems," *International journal for Numerical Methods in Engineering* 126, no. 7 (2025); e70022.

104. V. A. Buryachenko, "Unified Micromechanics Theory of Composites," arXiv:2503.14529v1, 1-89 2025.

105. V. A. Buryachenko, "Effective Nonlocal Behavior of Peridynamic Random Structure Composites Subjected to Body Forces With Compact Support and Related Prospective Problems," *Mathematics and Mechanics of Solids* 28 (2023): 1401–1436.

106. V. A. Buryachenko, "Effective Displacements of Peridynamic Heterogeneous Bar Loaded by Body Force With Compact Support," *International Journal for Multiscale Computational Engineering* 21 (2023): 27–42.

Appendix A

Forward and Backward Differences via Sine Polynomials

This Appendix develops trigonometric identities helpful in the main body of text.

We start from the angle addition and subtraction theorems

$$\sin(\varphi_1 + \varphi_2) = \cos\varphi_1 \sin\varphi_2 + \sin\varphi_1 \cos\varphi_2 \tag{A1}$$

$$\sin(\varphi_1 - \varphi_2) = -\cos\varphi_1 \sin\varphi_2 + \sin\varphi_1 \cos\varphi_2 \tag{A2}$$

for the sine function and angles $\varphi_1, \varphi_2 \in \mathbb{R}$. By subtracting these formulas, we obtain the expression

$$\sin(\varphi_1 + \varphi_2) - \sin(\varphi_1 - \varphi_2) = 2\cos\varphi_1 \sin\varphi_2 \quad \text{for} \quad \varphi_1, \varphi_2 \in \mathbb{R} \tag{A3}$$

We choose

$$\varphi_1 = \pi \frac{\left(j + \frac{1}{2}\right)k}{N} \quad \text{and} \quad \varphi_2 = \frac{k\pi}{2N}, \quad k = 1, 2, \ldots, N-1 \tag{A4}$$

and obtain the identity

$$\sin\left(\pi \frac{(j+1)k}{N}\right) - \sin\left(\pi \frac{jk}{N}\right) = 2\cos\left(\pi \frac{\left(j + \frac{1}{2}\right)k}{N}\right) \sin\left(\frac{k\pi}{2N}\right), \quad k = 1, 2, \ldots, N-1 \tag{A5}$$

Moreover, by inserting

$$\varphi_1 = \pi \frac{\left(j - \frac{1}{2}\right)k}{N} \quad \text{and} \quad \varphi_2 = \frac{k\pi}{2N}, \quad k = 1, 2, \ldots, N-1 \tag{A6}$$

we obtain the identity

$$\sin\left(\pi \frac{jk}{N}\right) - \sin\left(\pi \frac{(j-1)k}{N}\right) = 2\cos\left(\pi \frac{\left(j - \frac{1}{2}\right)k}{N}\right) \sin\left(\frac{k\pi}{2N}\right), \quad k = 1, 2, \ldots, N-1 \tag{A7}$$

In addition to the sine identities (A1), we also consider the cosine versions

$$\cos(\varphi_1 + \varphi_2) = \cos\varphi_1 \cos\varphi_2 - \sin\varphi_1 \sin\varphi_2 \tag{A8}$$

$$\cos(\varphi_1 - \varphi_2) = \cos\varphi_1 \cos\varphi_2 + \sin\varphi_1 \sin\varphi_2 \tag{A9}$$

that is, we are led to the equation

$$\cos(\varphi_1 + \varphi_2) - \cos(\varphi_1 - \varphi_2) = -2 \ \sin\varphi_1 \sin\varphi_2 \tag{A10}$$

We set (A4) to obtain the identity

$$\cos\left(\pi \frac{(j+1)k}{N}\right) - \cos\left(\pi \frac{jk}{N}\right) = -2\sin\left(\pi \frac{\left(j + \frac{1}{2}\right)k}{N}\right) \sin\left(\frac{k\pi}{2N}\right), \quad k = 1, 2, \ldots, N-1 \tag{A11}$$

Moreover, inserting (A6) yields the identity

$$\cos\left(\pi \frac{jk}{N}\right) - \cos\left(\pi \frac{(j-1)k}{N}\right) = 2\sin\left(\pi \frac{\left(j - \frac{1}{2}\right)k}{N}\right) \sin\left(\frac{k\pi}{2N}\right), \quad k = 1, 2, \ldots, N-1 \tag{A12}$$